Geochronology, 8, 547–565, 2026
https://doi.org/10.5194/gchron-8-547-2026

Meteoric beryllium-10 fluxes from soil inventory measurements in the East River watershed, Colorado, USA

José M. Marmolejo-Cossío[1], **Isaac J. Larsen**[1,2], **Eyal Marder**[1], **and Alan J. Hidy**[3]

[1]Department of Earth, Geographic, and Climate Sciences, University of Massachusetts, Amherst, 01003, USA
[2]Rocky Mountain Biological Laboratory, Crested Butte, CO, 81224, USA
[3]Center for Accelerator Mass Spectrometry, Lawrence Livermore National Laboratory, Livermore, CA, 94550, USA

Correspondence: Isaac J. Larsen (ilarsen@umass.edu)

Received: 30 August 2025 – Discussion started: 5 September 2025
Revised: 30 June 2026 – Accepted: 8 July 2026 – Published: 15 September 2026

Abstract. Meteoric beryllium-10 ($^{10}Be_{met}$) has a wide range of applications as a geochronometer and tracer of geological processes. $^{10}Be_{met}$ is produced in the atmosphere by cosmic rays and delivered to Earth's surface primarily via precipitation. $^{10}Be_{met}$ is particularly suitable for quantifying surface process rates where use of in situ-produced ^{10}Be is challenging, such as landscapes with quartz-poor bedrock. However, using $^{10}Be_{met}$ for dating and quantifying surface process rates requires constraining depositional fluxes across space and time. Although empirical and physical models for predicting fluxes exist, the predictions can deviate substantially from measured values. Here we quantify $^{10}Be_{met}$ flux in the East River watershed in Colorado, USA where precipitation is dominated by snowfall. We measured the $^{10}Be_{met}$ inventory in soils on five glacial moraines 13–18 ka in age that span 700 m of elevation and calculated $^{10}Be_{met}$ fluxes by dividing each inventory by moraine age. Inheritance-corrected fluxes range from 4.31×10^5–1.80×10^6 atoms cm^{-2} yr^{-1} and fluxes corrected using modeled erosional and desorption losses differ by a factor of 0.3 to 2.1. The predicted fluxes are well correlated with elevation, mean annual precipitation, mean snow depth, and snow water equivalent ($R^2 = 0.71$ to 0.99). Regression models applied to gridded elevation, precipitation, snow depth, and snow water equivalent data predict watershed-averaged fluxes of 1.1×10^6–3.8×10^6 atoms cm^{-2} yr^{-1}. Predicted fluxes from a published empirical model that estimates fluxes as a function of precipitation were 1.8–3.8 times higher than inheritance-corrected site fluxes, and 1.0 to 6.0 times higher than erosion- and desorption-corrected fluxes calculated using a profile-average desorption model. Fluxes predicted by general circulation models generally fall within the range of our empirically estimated watershed-averaged fluxes, although the degree of agreement depends on the predictor variable and whether inheritance-corrected or erosion- and desorption-corrected fluxes are used. Our results highlight both the importance of factors that drive variability in $^{10}Be_{met}$ delivery to soils and how local calibration can improve estimates of $^{10}Be_{met}$ flux in mountain watersheds.

1 Introduction

The cosmogenic nuclide beryllium-10 (^{10}Be) is used widely for geochronology and to quantify rates of Earth surface processes (Brown, 1984; Bierman and Nichols, 2004; Willenbring and von Blanckenburg, 2010; Granger et al., 2013). ^{10}Be forms during high energy collisions between cosmic particles and target nuclei (Lal and Peters, 1967). ^{10}Be produced in Earth's atmosphere (typically from N and O) is known as atmospheric, garden variety, or meteoric ^{10}Be ($^{10}Be_{met}$), whereas in situ-produced ^{10}Be ($^{10}Be_{in\ situ}$) is formed in mineral lattices at and near Earth's surface. Production rates of $^{10}Be_{in\ situ}$ are on the order of a few to tens of atoms g^{-1} yr^{-1} in quartz (Gosse and Phillips, 2001; Borchers et al., 2016). In contrast, $^{10}Be_{met}$ is generated at orders of magnitude higher rates, with a global-averaged flux in excess of 1 million atoms cm^{-2} yr^{-1}(Monaghan et al., 1986; McHargue and Damon, 1991). Prior to its deposition on Earth's surface by precipitation or dry fallout, $^{10}Be_{met}$ resides in the stratosphere and troposphere for 2 years and 55 d, respectively (Yamagata et al., 2019). Hence global circulation transports $^{10}Be_{met}$ from the site where it is produced in the atmosphere prior to its deposition (Field et al., 2006; Heikkilä et al., 2008). Once delivered to Earth's surface, $^{10}Be_{met}$ adsorbs to and is co-precipitated on mineral surfaces, hence the highest concentrations are associated with secondary minerals and fine-grained particles with high surface areas (e.g., Graly et al., 2010). $^{10}Be_{met}$ is partitioned with the solid phase at approximately neutral pH values (You et al., 1989). $^{10}Be_{met}$ is thought to be retained in soils where pH is $> \sim 4$ (Graly et al., 2010), but laboratory experiments indicate pH 6 soils are more retentive than pH 4 soils and that retention also varies as a function of the type of organic compounds present (Boschi and Willenbring, 2016a, b). $^{10}Be_{met}$ may be lost from upper soil horizons where low pH leads to leaching (Dixon et al., 2018), where clay minerals or humic material with adsorbed Be are translocated to greater depth (Pavich et al., 1984; Jagercikova et al., 2015), and where the surface of the soil has been eroded (Harden et al., 2002). Hence soil $^{10}Be_{met}$ inventories depend on a variety of factors, including the local delivery rate, landform age, degree of chemical weathering, soil pH, and erosion rate (e.g., Graly et al., 2010; Willenbring and von Blanckenburg, 2010).

The high production rates, which allow $^{10}Be_{met}/^{9}Be$ ratios to be readily measured via accelerator mass spectrometry (AMS), the wide range of soils and regolith where $^{10}Be_{met}$ is retained, and – unlike $^{10}Be_{in\ situ}$ – the ability to be measured in non-quartz-bearing materials has allowed $^{10}Be_{met}$ to be used widely as a geochronometer and tracer of Earth surface processes (e.g., Brown, 1987a, b; Graly et al., 2010; Willenbring and von Blanckenburg, 2010). For example, $^{10}Be_{met}$ has been used to date terraces and moraines (Tsai et al., 2008; Egli et al., 2010; Dünforth et al., 2012), determine rock-to-soil production rates (Monaghan et al., 1992; McKean et al., 1993; Jungers et al., 2009), quantify soil residence times (Monaghan et al., 1983; Bacon et al., 2012; Foster et al., 2015), determine earthflow velocities (Mackey et al., 2009), trace sediment through hillslopes and fluvial systems (Brown et al., 1988; Reusser and Bierman, 2010; West et al., 2014; Campforts et al., 2016), and, when coupled with ^{9}Be measurements, to quantify watershed-scale denudation rates and chemical weathering (von Blanckenburg et al., 2012; Wittmann et al., 2015; Dannhaus et al., 2018; Portenga et al., 2019; Deng et al., 2020b, 2021b). However, a requirement for using $^{10}Be_{met}$ for dating and quantifying surface process rates is that the deposition rate or flux of $^{10}Be_{met}$ (F_{met}, atoms $cm^{-2}\ yr^{-1}$) to the study area is known.

Numerous efforts have been made to measure or predict F_{met} at local to global spatial scales and over annual to millennial timescales (Willenbring and von Blanckenburg, 2010; Graly et al., 2011). Direct measurement of $^{10}Be_{met}$ concentrations in precipitation has been used to quantify $^{10}Be_{met}$ flux at point scales and short timescales to develop empirical relations that predict F_{met} as a function of precipitation rate or latitude (Brown et al., 1989; Monaghan et al., 1986; Raisbeck et al., 1981; Graham et al., 2003; Graly et al., 2011; Willenbring and von Blanckenburg, 2010). Nuclide production functions (e.g., Lal and Peters, 1967; Masarik and Beer, 1999) are coupled with general circulation models (GCM) to simulate global scale spatial and temporal patterns of F_{met} as a function of geomagnetic field strength, solar activity, atmospheric circulation, and precipitation (Field et al., 2006; Heikkilä et al., 2008; Heikkilä and von Blanckenburg, 2015; Panovska et al., 2023; Zheng et al., 2021, 2024). Millennial-averaged values of F_{met} can be inferred from soils by measuring the $^{10}Be_{met}$ inventory (I_{met}, atoms cm^{-2}) and dividing the inventory by landform age (e.g., Egli et al., 2010; Reusser et al., 2010; Graly et al., 2011; Deng et al., 2021a).

However, there is often disagreement between F_{met} values determined from soil inventories, global-scale physical models, and precipitation-based empirical models (Ouimet et al., 2015; Deng et al., 2020a; Krone et al., 2024). Substantial variability in F_{met}has been documented at spatial scales smaller than the grid cell size (often several hundred km) of many GCMs (Ouimet et al., 2015; Clow et al., 2020; Deng et al., 2020a). The discrepancies and spatial variability likely stem from temporal and spatial fluctuations in $^{10}Be_{met}$ production, atmospheric transport, and precipitation (Monaghan et al., 1986; Graham 2003; Jordan et al., 2003; Deng et al., 2020b; Krone et al., 2024). Hence, it is often desirable to locally-calibrate F_{met} prior to using $^{10}Be_{met}$to quantify surface process rates (e.g., Reusser et al., 2010; Ouimet et al., 2015; Deng et al., 2021a). Local-scale calibration is particularly important in mountainous settings, where microclimate variability can cause $^{10}Be_{met}$ inventories and fluxes to vary over short distances (Ouimet et al., 2015). Here we quantify the $^{10}Be_{met}$ flux at sites throughout the East River watershed, near Crested Butte, Colorado, USA (Fig. 1), a site of intensive research on the physical and biogeochemical drivers of watershed function (Hubbard et al., 2018). We measure $^{10}Be_{met}$ inventories on independently dated glacial moraines, assess local-scale influences on $^{10}Be_{met}$ flux, model potential losses of $^{10}Be_{met}$ due to erosion and desorption, and compare $^{10}Be_{met}$ flux measurements against predictions from empirical and physical models to evaluate the spatial variability and predictability of $^{10}Be_{met}$ fluxes in alpine environments.

2 Study Site

The East River drains the Elk Range of the Rocky Mountains in Colorado, USA ($\sim 38.9°$ N, $106.9°$ W). The East River joins the Taylor River to form the Gunnison River, a major tributary to the Colorado River. The East River watershed and its tributaries, Washington Gulch and the Slate River, are a steep mountainous landscape, with elevations that range from 2600 to 4100 m above sea-level (Fig. 2a). The climate is characterized by long, cold winters and cool, short summers (Hubbard et al., 2018). The mean annual temperature is ~ 0 °C, with mean minimum and maximum temperatures of -9.2 and 9.8 °C, respectively (Hubbard et al., 2018).

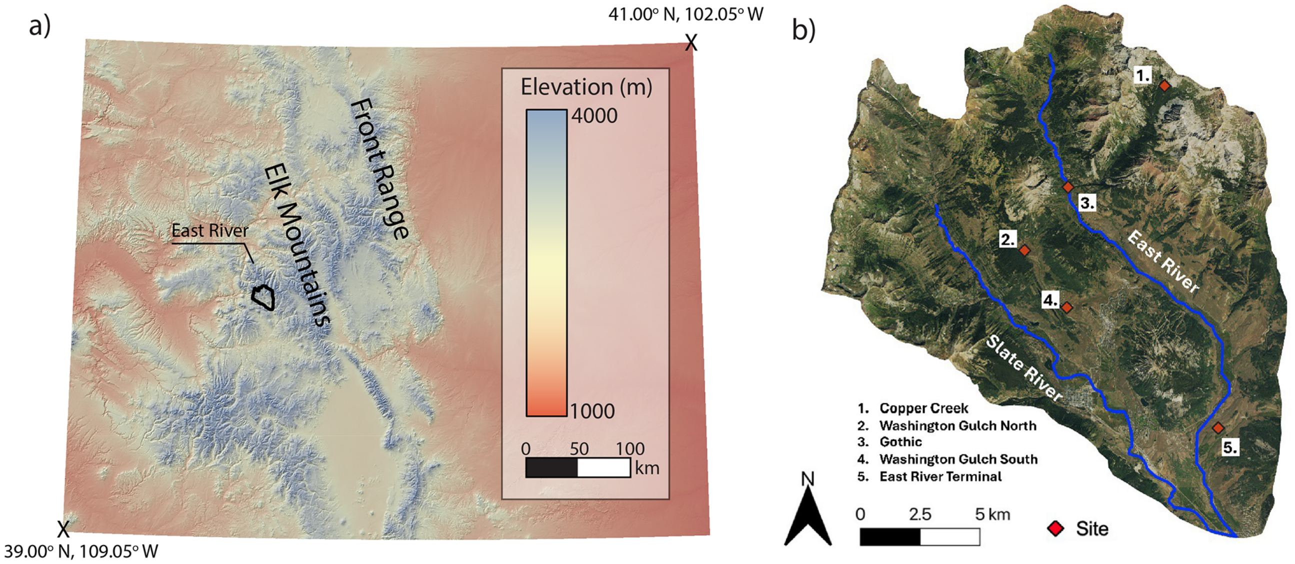

Figure 1. **(a)** Digital elevation model (DEM) of Colorado, USA showing the location of East River watershed. **(b)** Image of the East River watershed showing locations (red diamonds) where soil $^{10}Be_{met}$ inventories were measured.

Most of the annual precipitation occurs as snowfall, which can exceed several meters per year (Prather et al., 2023). Observations of enhanced precipitation rates on the windward side of mountains demonstrate that orography plays a strong role in controlling precipitation patterns within the watershed (Heflin et al., 2024). Hence like other mountain landscapes with orographically-influenced rain and snowfall (e.g., Roe, 2005), mean annual precipitation within the East River watershed increases with elevation (Fig. 2). The continental subarctic climate in the East River watershed supports montane, subalpine, and alpine ecosystems, which host aspen, meadow, mixed conifer, sagebrush, grass, sedge, and forb species (Fig. S1 in the Supplement) (Harte and Shaw, 1995). Bedrock in the watershed is primarily Cretaceous-age Mancos Shale and other sedimentary rocks that are intruded by Paleocene- to Miocene-age quartz monzonite porphyry and granodiorite rocks (Gaskill et al., 1967, 1991). Pleistocene glaciers eroded high elevation cirques and deposited moraines and outwash in the main East River valley (Gaskill et al., 1967, 1991). Exposure ages based on $^{10}Be_{in\ situ}$ concentrations measured in samples from boulders indicate the terminal moraine at the end of the valley dates to 17.9 ka, whereas the youngest recessional moraine in a high-elevation cirque within the Copper Creek watershed was exposed at 13.0 ka (Quirk et al., 2024).

3 Methods

3.1 Field and laboratory methods

Soil $^{10}Be_{met}$ inventories were determined for five glacial moraines with exposure ages that range from 17.9 to 13.0 ka (Fig. 1; Table 1; Quirk et al., 2024). Soil pits were dug on the flattest part of each moraine crest to minimize the potential of post-depositional erosion, with the exception of the Gothic moraine site, which was opportunistically located where the East River has laterally eroded a cutbank into the moraine, permitting deeper sampling. The pits were dug until shovel refusal, to depths between 60 and 145 cm. At the Washington Gulch North site, we sampled from a soil pit on a flat portion of the moraine, and collected a sample on the same moraine that was exposed by a recent landslide ∼ 375 m from the soil pit to assess inheritance in a deeper sample than we could access by digging. Bulk density was determined at each site by driving a 90.8 cm^3 steel cylinder into the soil at depths corresponding to different horizons and weighing the dry soil (Table S1 in the Supplement). Samples were collected in either 5 or 10 cm depth increments by pressing a stainless-steel box, open at the top and front, into the face of the soil pit and scraping soil into the box. Samples were dried and sieved to separate < 2 mm particles. We combined samples from adjacent depths to generate composite samples that encompassed depth intervals that range from 10 to 20 cm. Samples were combined by mixing splits of the < 2 mm size fraction in proportion to the total mass of < 2 mm particles in each sampling interval. The combined < 2 mm fractions were powdered using a tungsten carbide shatter box. We measured soil pH in water and in 0.01 M $CaCl_2$ to assess $^{10}Be_{met}$ retention. The measurements in water were made by mixing ∼ 5 g of powdered < 2 mm grain-size material with 12 mL ultrapure water. The $CaCl_2$ pH measurements were made by mixing approximately 5 g of powdered < 2 mm material with 25 mL of 0.01 M $CaCl_2$ to maintain a 1 : 5 soil to solution ratio (You et al., 1989). The pH values were measured with a Fisher Scientific accumet AE150 probe calibrated with mul-

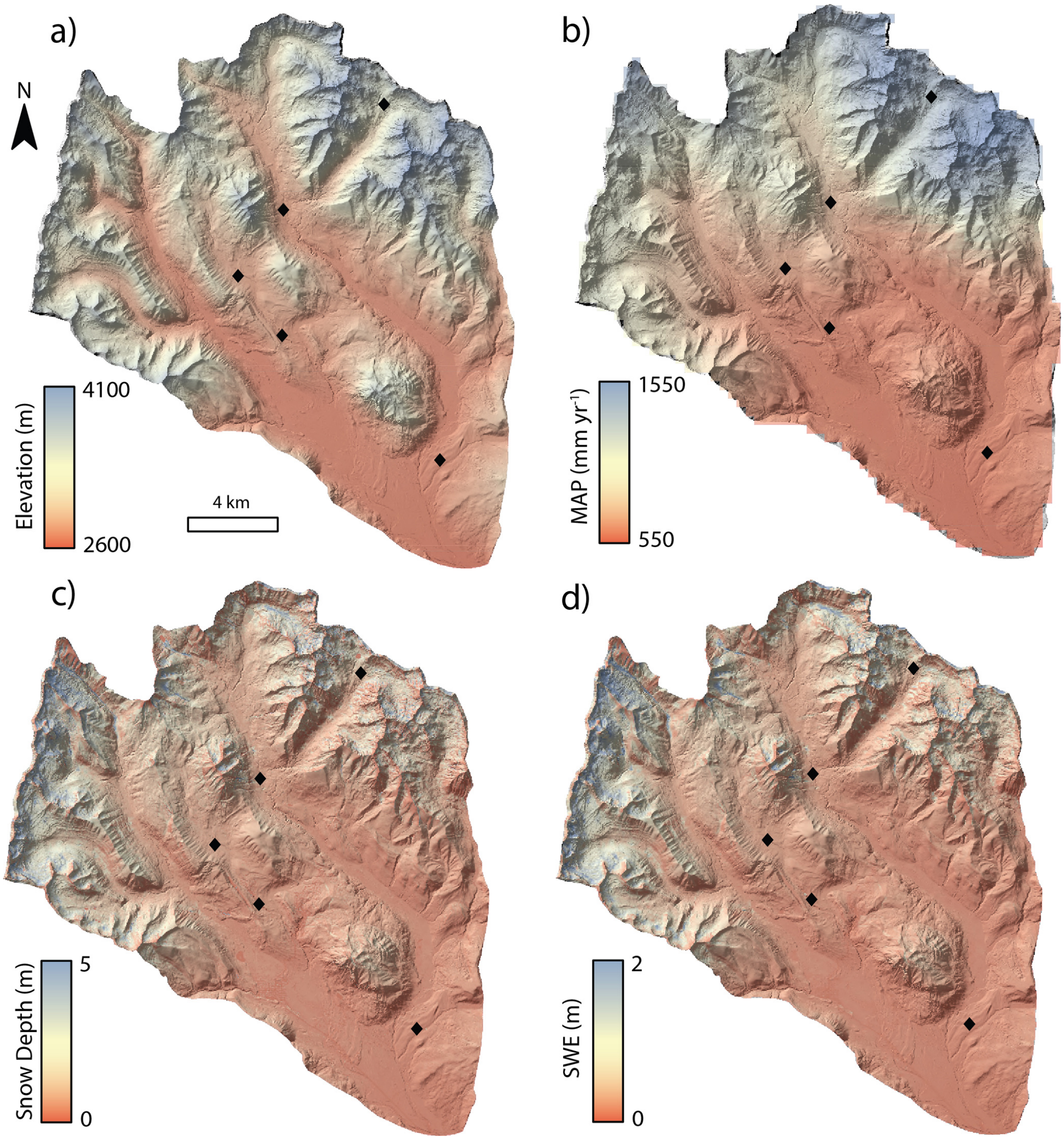

Figure 2. Maps of environmental variables within the East River watershed. **(a)** LiDAR-derived elevation data (Goulden et al., 2020); **(b)** downscaled Parameter-elevation Regressions on Independent Slopes Model (PRISM) mean annual precipitation (MAP) data averaged from 2008–2019 (Mital et al., 2022); **(c)** mean snow depth, and **(d)** mean snow water equivalent (SWE), derived from Airborne Snow Observatory data from 2018–2019 (Painter, 2018a, b). The black diamonds show each sample location.

tiple U.S. National Institute of Standards and Technology-traceable standards immediately prior to use (for more details, please see Table S2).

Sample locations were determined using a Bad Elf Flex GNSS with sub-meter precision. Slope and curvature values (Fig. S2) were generated using 3 m LiDAR DEM (Goulden et al., 2020). Curvature (m^{-1}) was derived by fitting a polynomial surface to a neighbourhood of 11 pixels using LSD-topotools (Mudd et al., 2014). Surface erosion rate (dz/dt) values were measured for the Gothic moraine site using an in situ-produced ^{10}Be depth profile (Quirk et al., 2024) and modelled for the other sites using Eq. (4).

$^{10}Be_{met}$ chemistry was conducted at the University of Massachusetts Cosmogenic Nuclide Laboratory using the Stone (1998) fusion method. Approximately 0.5 g of homogenized and pulverized < 2 mm soil particles was weighed into 30 mL Pt crucibles. We then added ~ 350 µg of ^{9}Be from a carrier with a $^{10}Be/^{9}Be$ ratio of $\sim 1.75 \times 10^{-15}$ to each sample. We also added 1000 µg of Al from a commercial carrier, which reportedly improves Be yields (Stone and Balco, 2004). Samples were dried overnight at 60 °C, then mixed with ~ 2.5 g of KHF_2 and ~ 0.5 g of Na_2SO_4 flux prior to heating with a gas torch to melt the sample. Once the samples were fully melted, they were heated for an ad-

Table 1. Age, location, topographic attributes, and estimated surface lowering rates for the sites used to assess meteoric ^{10}Be flux.

Moraine	Age (ka)	Latitude	Longitude	Slope (°)	Curvature (m^{-1})	dz/dt ($mm\,yr^{-1}$)
Copper Creek	13.0 ± 0.1	39.001190	−106.940171	7.0	0.00	0.000
Washington Gulch North	17.9 ± 0.2	38.930916	−107.013397	2.0	−0.03	−0.017
Gothic moraine	14.0 ± 1.0	38.957877	−106.990814	4.3	−0.04	−0.023
Washington Gulch South	17.3 ± 0.1	38.907394	−106.990058	0.5	−0.01	−0.006
East River terminal	17.8 ± 0.2	38.858632	−106.907514	4.0	−0.02	−0.012

ditional 1–2 min. Be was extracted by soaking the crucibles with the fusion cakes overnight in 200 mL of ultrapure water. The solution was reduced to a volume of ∼ 30 mL by evaporation, then centrifuged. We decanted the supernatant and added ∼ 10–15 mL of 49 % $HClO_4$ to precipitate K as $KClO_4$. The solution was centrifuged to remove $KClO_4$ and the supernatant was dried overnight in Teflon beakers following addition of 1 mL of 8 M HNO_3. The samples were redissolved in 25 mL ultrapure water and Be was precipitated as BeOH by adding drops of ∼ 10 % NH_4OH until the solution pH was ∼ 9. The $Be(OH)_2$ was washed multiple times by repeatedly centrifuging, pouring off the supernatant, and remixing the $Be(OH)_2$ with ultrapure water. The $Be(OH)_2$ was dissolved with 2–3 drops of 6 M HCl, dried overnight in a quartz crucible, calcined by heating with a gas torch until BeO remained incandescent for 1 min, and packed into cathodes with Nb powder. The $^{10}Be/^{9}Be$ ratios were analyzed by AMS at Lawrence Livermore National Laboratory (LLNL) against AMS Be standard 01-5-4 (LLNL standard 07KNSTD) (Nishiizumi et al., 2007). ^{10}Be concentrations in soil samples were blank-corrected by subtracting $^{10}Be/^{9}Be$ ratios measured in full process blanks from ratios measured in samples, with uncertainties added in quadrature.

Primary and secondary soil minerals contain ^{9}Be at parts-per-million concentrations (e.g., Barg et al., 1997; Bacon et al., 2012). To assess the amount of naturally-occurring ^{9}Be relative to the amount added as carrier, we dissolved ∼ 0.1 g of each sample in 49 % HF, reconstituted the samples in a 1 % HNO_3 + 1 % H_2SO_4 solution, centrifuged to separate insoluble organic matter, and measured Be in the supernatant via Inductively Coupled Plasma – Optical Emission Spectroscopy (ICP-OES).

3.2 $^{10}Be_{met}$ inventory and flux analysis

We determined millennial-averaged F_{met} values for each moraine by measuring the $^{10}Be_{met}$ inventory. The inventory was determined by multiplying the inheritance-corrected $^{10}Be_{met}$ concentration (N_{corr}, atoms g^{-1}), by soil bulk density (ρ, $g\,cm^{-3}$), the thickness of the sampling interval (z, cm), and the volumetric fraction of fine (< 2 mm) soil V_f, and summing the values for all (n) individual sample depth increments (i) (e.g., Deng et al., 2021a):

$$I_{met} = \sum_{i=1}^{n} (N_{corr} \cdot \rho \cdot z \cdot V_f)_i. \tag{1}$$

Using soil inventories to quantify F_{met} assumes that $^{10}Be_{met}$ accumulation begins at the time a landform is initially exposed to wet and dry fallout. However, the ages of the moraines we use to constrain flux are orders of magnitude lower than the ^{10}Be half-life (1.387 Ma; Chmeleff et al., 2010; Korschinek et al., 2010). Hence the soils we collected contain inherited $^{10}Be_{met}$ atoms that were sorbed to mineral surfaces prior to their incorporation within the moraines. The inherited concentration was identified, following methods from prior work (e.g., Reusser et al., 2010), by the presence of a near constant $^{10}Be_{met}$ concentration in the lower part of the depth profile. At four of the five sites, the $^{10}Be_{met}$concentration reached a near-constant value with depth (Fig. 3). We assumed the concentration measured in the lowest depth interval was equal to the inherited $^{10}Be_{met}$concentration and subtracted that value from concentrations measured in overlying samples (e.g., Reusser et al., 2010) and added the 1σ AMS analytical uncertainties in quadrature. If the $^{10}Be_{met}$concentration in the sample used for the inheritance correction was greater than the concentration of a sample higher in the profile (e.g., at the Gothic moraine site), we set the concentration for that depth interval to zero. At the fifth site in the Copper Creek watershed, the $^{10}Be_{met}$ profile is well-mixed above an indurated stone line at the base of the soil (Fig. 3a). Hence, we used the mean inheritance value of 7.58×10^{7} atoms g^{-1} measured at the other four sites to correct for inheritance at the Copper Creek site.

Since we measured bulk density by soil horizon, and not sample depth interval, we assigned bulk density values to each sample interval based on soil horizons identified in the field (Table S3). The volumetric fraction of < 2 mm soil particles was calculated for each depth interval following Deng et al. (2021a) as: $V_f = (1 - V_{c1}) \times (1 - V_{c2})$, where V_{c1} and V_{c2} are volumes of two sizes of coarse clasts. V_{c1} was determined by sieving each sample to separate < 2 and > 2 mm clasts and the volume fraction of > 2 mm clasts was calculated assuming a density of 2.65 $g\,cm^{-3}$. V_{c2} was estimated by using field photos of each soil pit to digitize the area of large cobble- to boulder-sized clasts that were too large to be sampled by our 44.7 mm diameter steel ring. The volume

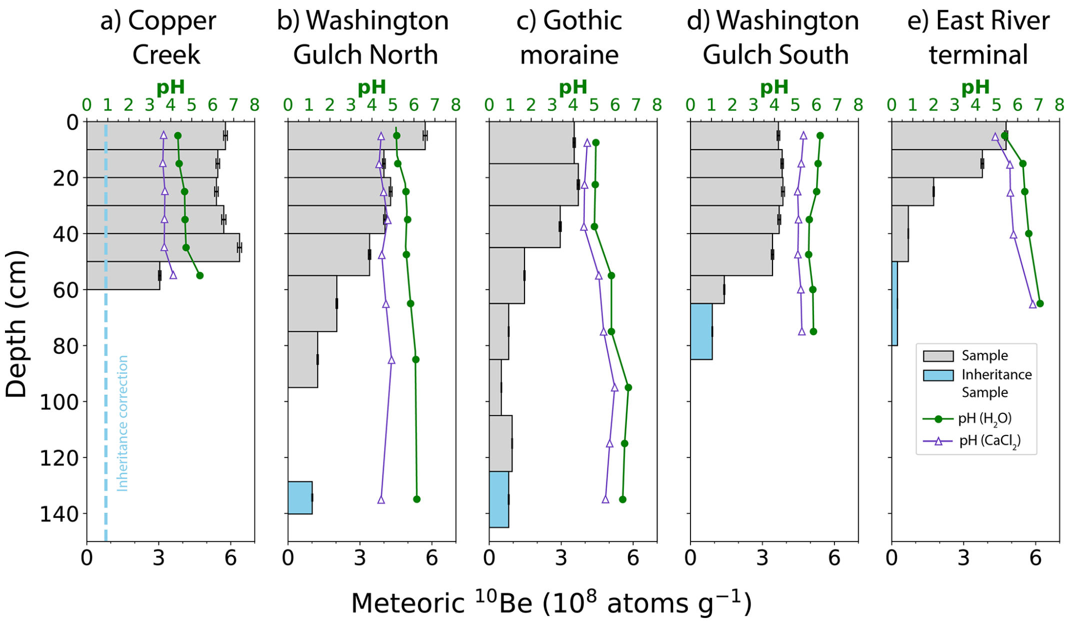

Figure 3. $^{10}Be_{met}$concentration and pH as a function of depth for **(a)** Copper Creek, **(b)** Washington Gulch North, **(c)** Gothic, **(d)** Washington Gulch South, and **(e)** East River Terminal moraines. Grey boxes show measured concentrations and uncertainties. Blue boxes indicate samples assumed to represent the inherited $^{10}Be_{met}$ concentration. In **(a)**, the blue dashed line shows the mean inheritance value calculated from profiles **(b)**–**(e)**. The sample used for the inheritance correction in **(b)** was sampled from a landslide exposure on the Washington Gulch North moraine that was 374 m away from the soil pit where the other samples were collected.

fraction of large clasts was calculated by multiplying the area fraction by two-thirds (e.g., Deng et al., 2021a). We propagated uncertainty for individual depth increments by adding uncertainty associated with the inheritance-corrected $^{10}Be_{met}$ concentrations and an assumed 5 % relative uncertainty in both ρ and V_f, in quadrature.

Given that the age of the moraines we sample is much less than the mean life of ^{10}Be, and hence loss via decay is negligible, we divided the I_{met} value by moraine age (t, years) to determine the flux (e.g., Graly et al., 2010; Reusser et al., 2010; Ouimet et al., 2015; Clow et al., 2020; Deng et al., 2021a):

$$F_{met} = \frac{I_{met}}{t}. \qquad (2)$$

Uncertainty in F_{met} for each calibration site was calculated by adding uncertainty in I_{met} values and moraine age in quadrature. Moraine age uncertainty was based on the standard error of the mean of multiple exposure ages on boulders or, for the Gothic moraine, a 1 ka uncertainty associated with a $^{10}Be_{in\ situ}$ depth profile age (Table 1; Quirk et al., 2024).

The F_{met} values calculated using Eq. (2) assume complete retention of $^{10}Be_{met}$. We corrected fluxes (F_{cor}) for erosional and desorption losses according to Clow et al. (2020):

$$F_{cor} = (\epsilon \cdot N_{surface}) + (I_{met} \cdot \lambda) + \left(Q \times N_j / K_{d,j}\right), \qquad (3)$$

where ϵ is the erosion rate (g cm^{-2} yr^{-1}), $N_{surface}$ is the inheritance-corrected $^{10}Be_{met}$ concentration in the uppermost sample that is assumed to represent the concentration in eroding soil (atoms g^{-1}), λ is the ^{10}Be decay constant (4.998×10^{-7} yr^{-1}), Q (L cm^{-2} yr^{-1}) is the flux of water through the soil, and N_j and $K_{d,j}$ are the inheritance-corrected $^{10}Be_{met}$ concentration and Be partition coefficient (L kg^{-1}), respectively, for the soil depth interval j of interest, which is described below.

The $^{10}Be_{in\ situ}$ depth profile method used to date the Gothic moraine, which was also sampled for $^{10}Be_{met}$, yielded a median dz/dt value of -2.3×10^{-5} m yr^{-1} (Quirk et al., 2024). The source area for the Gothic moraine is primarily intrusive rock, hence the till matrix contained sufficient quartz for $^{10}Be_{in\ situ}$ measurement. However, the till matrix was dominated by quartz-poor Mancos shale at the other sites and because of the dense shale-derived matrix, the pits could not be excavated deep enough to permit use of a $^{10}Be_{in\ situ}$ profile to assess erosion rates. Hence we modeled the surface lowering rate at the other sites as:

$$\frac{dz}{dt} = D\nabla^2 z, \qquad (4)$$

where D is the topographic diffusion coefficient (m^2 yr^{-1}), and $\nabla^2 z$ is topographic curvature (m^{-1}). Equation (4) is appropriate for low-gradient hillslopes like the moraines we sampled (Table 1), where surface lowering rates scale linearly with curvature (e.g., Kwang et al., 2022). Based on the median surface lowering rate and topographic curvature (Table 1), we infer the value of D at the Gothic moraine site is

$5.8 \times 10^{-4}\,\mathrm{m}^2\,\mathrm{yr}^{-1}$. Given the similar soils and climate, we assume D is comparable across the five moraines and use the diffusion coefficient for the Gothic moraine site and topographic curvature values to estimate $\mathrm{d}z/\mathrm{d}t$ values at the four sites that lack direct measurements. We assume $\mathrm{d}z/\mathrm{d}t$ values from Eq. (4) are equivalent to ϵ values in Eq. (3) and convert from units of length per time to mass per area per time using bulk density values inferred for the N_{surface} sample (Table S3).

We calculate Q as the difference between mean annual precipitation (MAP) and evapotranspiration (ET), which assumes that only the fraction of the precipitation that infiltrates the entire soil profile contributes to desorption losses. We determined MAP at each site using downscaled (400×400 m) Parameter-elevation Regressions on Independent Slopes Model (PRISM; Daly et al., 2008) raster data, which averages over the period from 2008–2019 (Mital et al., 2022). We used annual ET data from 2014–2015 that were simulated using the Community Land Model (CLM). ET values were reported for discrete locations within the East River watershed (Tran et al., 2019) and we assigned values to our study sites using the CLM prediction with an elevation and vegetation that most closely matched each site (Table S4). Following Deng et al. (2021a), we estimated K_d values using a logistic regression relationship from Campforts et al. (2016) where K_d is predicted as a function of pH measured in H_2O.

Prior work used Eq. (3) to assess $^{10}\mathrm{Be}_{\mathrm{met}}$ desorption losses from the surface of the soil profile and assumed that desorbed Be exited the profile (Clow et al., 2020). Here we model three different desorption scenarios where N_j and $K_{\mathrm{d},j}$ correspond to values for different depth intervals. The first analysis we conducted is for the soil surface sample, which yields results comparable to those of Clow et al. (2020). The second analysis uses profile-average values of N and K_d and assumes the mean K_d for the entire soil column is the primary influence on desorption losses. Because pH generally increases with depth, the third scenario uses K_d values for the lowermost sample in the profile and assumes desorption losses are controlled by the pH of the lowermost depth increment in the profile. The soil surface and lowermost sample scenario uses the respective K_d value and inheritance-corrected $^{10}\mathrm{Be}_{\mathrm{met}}$ concentration associated with each depth interval for N_j. The profile-average scenario uses the weighted mean K_d value for the entire profile and the profile weighted mean value of the inheritance-corrected $^{10}\mathrm{Be}_{\mathrm{met}}$ concentration for N_j, where the thickness of each sampling interval was used as the weighting factor. We report the results from all scenarios, but use the results of the profile-average scenario for regression analyses and for comparison against predictions from existing empirical and GCM-based models.

3.3 Relationships between flux, elevation, and precipitation

It is well-established that the flux of $^{10}\mathrm{Be}_{\mathrm{met}}$ is strongly influenced by precipitation rates (e.g., Willenbring and von Blanckenburg, 2010; Graly et al., 2011). Given that precipitation within the East River watershed is orographically-controlled (Heflin et al., 2024), there should also be a relationship between elevation and the flux of $^{10}\mathrm{Be}_{\mathrm{met}}$. We used gridded datasets and univariate regression to assess the correlation between F_{met} (and F_{cor}) and elevation, MAP, snow depth, and snow water equivalent (SWE). The influence of elevation was evaluated using 3 m resolution LiDAR data (Goulden et al., 2020). We used the same gridded MAP data described in Sect. 3.2 that we use to estimate Q (Mital et al., 2022), and snow data products derived from the Airborne Snow Observatory (ASO; Painter et al., 2016). ASO combines airborne LiDAR and imaging spectrometry with snow energy balance models to generate spatial maps of snowpack properties. Snow depth is calculated as the difference between a snow-covered LiDAR survey and a snow-free "bare-earth" LiDAR scan. For this study, we used ASO-derived snow depth data (3 m resolution) acquired on 31 March 2018, and 7 April 2019 (Painter, 2018a). We used SWE data (50 m resolution) from the same dates as snow depth (Painter, 2018b). We used the coefficient of determination (R^2) from linear regression analysis to assess the degree that variability in F_{met} and F_{cor} is explained by elevation and precipitation metrics. The significance of each regression model was determined using the associated p value. For the precipitation-based metrics, we additionally conducted regression through the origin analyses where the y-intercept was set to equal zero, because F_{met} and F_{cor} should be zero where precipitation is zero, assuming dry fallout of $^{10}\mathrm{Be}_{\mathrm{met}}$ is negligible.

3.4 Comparing inventory-based fluxes against estimates from other methods

We predicted F_{met} for each of the five calibration sites using the precipitation- and latitude-based empirical model of Graly et al. (2011) using the down-scaled PRISM MAP data (Mital et al., 2022). We re-scaled the Graly et al. (2011) predictions, which are based on present-day precipitation measurements, to Holocene-averaged values by multiplying them by $1/0.67$ to account for differences in paleomagnetic and solar intensity variations (e.g., Clow et al., 2020) and compared the re-scaled predictions against our F_{met} and F_{cor} values.

The elevation, MAP, snow depth, and SWE data for each sample location were extracted from gridded datasets that span the entire watershed, including the Washington Gulch and Slate River tributaries. We applied the regression equations described in Sect. 3.3 to generate a prediction of flux for each pixel in the watershed. We then predicted watershed-average fluxes by calculating the mean value of all pixels.

We used the regression through the origin models to generate predictions based on MAP, snow depth, and SWE to ensure model predictions were physically realistic (e.g., a negative y-intercept value could produce a negative flux value, which is physically-implausible). Our predicted watershed-average flux values integrate over a larger area, hence they are more appropriate for comparison against GCM-based flux estimates than our point-based values from each soil pit.

We compared our watershed-averaged flux predictions against three GCM-based predictions. The ECHAM5-HAM flux predictions of Heikkilä and von Blanckenburg (2015) are from a three-decade simulation that used pre-industrial aerosol and greenhouse gas concentrations and a modern solar modulation factor (φ) of 501.76 MeV. The solar modulation during the Holocene was lower ($\varphi = 280.94$ MeV), hence Heikkilä and von Blanckenburg (2015) multiplied the fluxes by a factor of 1.23 to re-scale them to average Holocene values that represent the last 9400 years. The GEOS-Chem 14.1.1 and ECHAM6.3-HAM2.3 model predictions of Zheng et al. (2024) are modern predictions that average from 2005 to 2013 and use a φ value of 488 MeV. Since our flux estimates from the East River average over the Holocene, we multiply both of the Zheng et al. (2024) flux predictions by 1.23, which approximately re-scales them to Holocene-averaged values and makes them more comparable to our predicted watershed-average values.

4 Results

4.1 Soil pH

Soil pH for the uppermost sample interval of each profile ranged from 4.3–6.3 when measured in H_2O and from 3.7–5.4 when measured in $CaCl_2$ and the values generally increased with depth (Fig. 3; Table S2). Mean pH values averaged across all depths for Copper Creek, Washington Gulch North, Gothic, Washington Gulch South, and East River Terminal moraines are 4.7, 5.6, 5.7, 5.9, and 6.3, for measurements in H_2O, and 3.8, 4.6, 5.2, 5.2, and 5.8, when measured in $CaCl_2$, respectively. The most acidic soils are found at the Copper Creek site, which has the highest elevation and is dominated by spruce-fir forest vegetation (Fig. S1).

4.2 $^{10}Be_{met}$ profiles, inventories, fluxes, and controls on fluxes

AMS-measured $^{10}Be/^{9}Be$ ratios typically were on the order of 1.0×10^{-12} to 10×10^{-12}, which is several orders of magnitude greater than the 2×10^{-15} to 5×10^{-15} ratios measured in blanks (Table 2). Measured $^{10}Be_{met}$ concentrations ranged from about 2.4×10^{7} to 6.4×10^{8} atoms g^{-1} (Table 2). Concentrations of ^{9}Be were ~ 1 ppm indicating the average mass of ^{9}Be in the samples was ~ 0.2 % of the mass added as carrier (Table S5). Given that 0.2 % is less than the uncertainty of the Be concentration of the carrier we used (1.2 %), no corrections were made to the AMS-measured $^{10}Be/^{9}Be$ ratios. The $^{10}Be_{met}$ concentration profiles exhibit a variety of shapes. Profiles at four of the sites have relatively uniform concentrations in the upper ~ 0.5 m of the profile, with maximum concentrations at or near the ground surface that decline at greater depths (Table 2; Fig. 3a–d). At the lowest elevation site on the terminal moraine, the $^{10}Be_{met}$ concentration is greatest at the surface and declines exponentially with depth (Fig. 3e). The shallowest profile was at the Copper Creek site, where a coarse, indurated stone layer 60 cm below the ground surface prevented deeper sampling. At Copper Creek the concentration profile is well mixed in the upper 40 cm, exhibits a subsurface peak concentration 40–50 cm below the ground surface, and then declines sharply in the 10 cm interval directly above the stone line, but not to levels as low as those observed in the deepest samples from other profiles (Fig. 3a). Inheritance-corrected $^{10}Be_{met}$ inventories range from 7.68×10^{9} to 2.35×10^{10} atoms cm^{-2} (Table 3), with the largest and smallest inventories at the Copper Creek and East River terminal moraine sites, respectively. Inheritance-corrected F_{met} values range from 0.43×10^{6} to 1.80×10^{6} atoms cm^{-2} yr^{-1} (Table 3). Correcting for inheritance, erosion, desorption (using the profile averaged model), and decay yields F_{cor} values of 0.31×10^{6} to 3.7×10^{6} atoms cm^{-2} yr^{-1} (Table 4). Hence accounting for erosion and desorption caused fluxes to deviate from uncorrected values by a factor of 0.3 to 2.1 (Tables 3, 4). The desorption model scenarios for the uppermost and lowermost soil depth intervals predict fluxes that are generally within a factor of two of the profile-averaged model, except for the Copper Creek site, where the flux predicted from the upper sample pH is an order of magnitude greater than the flux predicted by the pH of the lowermost sample (Table 4).

F_{met} values are well-correlated with elevation and precipitation metrics in the East River watershed (Fig. 4; Table S6). F_{met} values are linearly correlated with elevation ($R^2 = 0.91$), mean annual precipitation ($R^2 = 0.82$–0.85), mean snow depth ($R^2 = 0.95$–0.97), and mean SWE ($R^2 = 0.97$–0.98). Due to the large range of elevation and precipitation within the watershed (Fig. 2), the regression models predict substantial within-watershed variability in F_{met} (Fig. 5). The erosion- and desorption-corrected fluxes based on the profile-averaged model exhibit similar trends with elevation and precipitation variables, but the correlations exhibited greater variability, with R^2 values of 0.96 for elevation, 0.56–0.95 for mean annual precipitation, 0.72–0.88 for mean snow depth in 2018–2019, and 0.66 to 0.90 for mean SWE in 2018–2019 (Fig. 4). The Copper Creek site has substantially higher elevation and precipitation values than the other sites and hence strongly influences regression relationships. When the Copper Creek site is omitted from the analysis, R^2 values range from 0.25 to 0.93 (Table S7).

The different regression models predicted watershed-averaged F_{met} values that vary by about a factor of two (Table 5). For elevation, the regression models yield average

Table 2. $^{10}Be_{met}$ sample information and AMS results.

Site	Sample ID[a] (LLNL BE number)	Sample mass (g)	^{9}Be added as carrier (µg)	$^{10}Be:^{9}Be$ ratio ($\times 10^{-12}$)	$^{10}Be:^{9}Be$ ratio uncertainty ($\times 10^{-14}$)	^{10}Be concentration and uncertainty[b] (10^6 atoms g^{-1})	Inheritance-corrected ^{10}Be concentration and uncertainty (10^6 atoms g^{-1})
Copper Creek	ER_CCT_pit_1_0-10 (BE54737)	0.5227	353.3	12.8	8.50	578.0 ± 7.9	502.2 ± 8.0
	ER_CCT_pit_1_10-20 (BE54738)	0.5396	352.9	12.5	8.25	546.1 ± 7.4	470.3 ± 7.6
	ER_CCT_Pit_1_20_30 (BE54926)	0.5174	351.7	11.9	8.08	540.4 ± 7.4	464.6 ± 7.5
	ER_CCT_pit_1_30-40 (BE54740)	0.4994	352.9	12.1	11.5	571.2 ± 8.7	495.4 ± 8.8
	ER_CCT_pit_1_40-50 (BE54741)	0.4998	352.9	13.5	8.95	636.8 ± 8.7	561.0 ± 8.8
	ER_CCT_pit_1_50-60 (BE54743)	0.5004	352.2	6.47	7.15	304.2 ± 4.9	228.4 ± 5.1
Washington Gulch North	ER_S2_pit_1_0-10 (BE54729)	0.5456	353.8	13.2	1.16	571.9 ± 8.5	464.7 ± 8.7
	ER_S2_pit_1_10-20 (BE54730)	0.5366	353.3	9.09	6.58	399.8 ± 5.6	292.6 ± 5.9
	ER_S2_pit_1_20-30 (BE54731)	0.5165	352.2	9.39	6.71	427.7 ± 5.9	320.6 ± 6.2
	ER_S2_pit_1_30-40 (BE54732)	0.4948	353.5	8.47	6.13	404.2 ± 5.6	297.0 ± 6.0
	ER_S2_pit_1_40-55 (BE54733)	0.4992	353.4	7.19	5.21	340.0 ± 4.7	232.8 ± 5.1
	ER_S2_pit_1_55-75 (BE54735)	0.5032	352.4	4.35	4.15	203.4 ± 3.1	96.3 ± 3.7
	ER_S2_pit_1_75-95 (BE54736)	0.4959	353.1	2.60	4.82	123.6 ± 2.7	16.4 ± 3.3
	ER24_S2_Pit_2_130-140_A (BE55950)	0.5249	351.1	2.40	3.29	107.2 ± 1.9	0 ± 0
Gothic	ER_GM_pit_1_0-15 (BE54756)	0.4996	352.3	7.52	4.88	354.2 ± 4.8	273.0 ± 5.1
	ER_GM_pit_1_15-30 (BE54758)	0.4975	350.6	7.89	4.06	371.4 ± 4.8	290.2 ± 5.1
	ER_GM_pit_1_30-45 (BE54759)	0.4983	351.9	6.27	5.5	295.7 ± 4.4	214.6 ± 4.7
	ER_GM_pit_1_45-65 (BE54760)	0.5025	352.1	3.14	3.65	146.9 ± 2.4	65.7 ± 3.0
	ER_GM_pit_1_65-85 (BE54761)	0.5308	354.6	1.82	2.93	90.9 ± 1.5	9.8 ± 2.3
	ER_GM_pit_1_85-105 (BE54762)	0.5149	351.3	1.11	1.99	50.5 ± 1.1	0 ± 0
	ER_GM_pit_1_105-125 (BE54765)	0.5073	352.1	2.06	1.81	95.4 ± 1.4	14.2 ± 2.3
	ER_GM_pit_1_125-145 (BE54766)	0.5174	351.7	1.79	3.31	81.2 ± 1.8	0 ± 0
Washington Gulch South	ER_AM_Pit_1_0_10 (BE54780)	0.4927	353.0	7.66	6.72	366.6 ± 5.4	275.6 ± 5.6
	ER_AM_pit_1_10-20 (BE54750)	0.4863	352.6	7.89	5.23	382.1 ± 5.2	291.2 ± 5.4
	ER_AM_pit_1_20-30 (BE54751)	0.5008	352.0	8.21	9.03	385.5 ± 6.2	294.5 ± 6.4
	ER_AM_pit_1_30-40 (BE54752)	0.5210	351.8	8.20	8.53	369.9 ± 5.8	278.9 ± 6.0
	ER_AM_pit_1_40-55 (BE54753)	0.5648	351.7	8.22	7.34	341.9 ± 5.1	251.0 ± 5.3
	ER_AM_pit_1_55-65 (BE54754)	0.5088	352.0	3.05	3.07	140.9 ± 2.2	49.9 ± 2.7
	ER_AM_pit_1_65-85 (BE54755)	0.5308	354.6	2.04	2.34	90.9 ± 1.5	0 ± 0
East River Terminal	ER_BCTM_pit_1_0-10 (BE54744)	0.4968	351.1	10.1	7.34	476.8 ± 6.7	452.9 ± 6.7
	ER_BCTM_pit_1_10-20 (BE54745)	0.4980	352.2	8.00	7.02	377.9 ± 5.6	354.0 ± 5.6
	ER_BCTM_pit_1_20-30 (BE54746)	0.5889	353.0	4.37	3.72	174.9 ± 2.6	151.0 ± 2.6
	ER_BCTM_pit_1_30-50 (BE54747)	0.4999	353.0	1.47	1.65	69.2 ± 1.1	45.3 ± 1.3
	ER_BCTM_pit_1_50-80 (BE54748)	0.4902	352.9	0.500	9.27	23.9 ± 0.53	0 ± 0

[a] Values at the end of each sample ID refer to the sample depth interval (cm). [b] Reported ^{10}Be concentrations are corrected using $^{10}Be/^{9}Be$ ratios measured in process blanks. $^{10}Be/^{9}Be$ ratios measured in process blanks in the same batches as the samples were: 2.44, 1.64, 2.55, 2.93, 2.11, 2.39, 4.71, 2.92, and 2.70×10^{-15}. Uncertainty in I_{met} values was determined by adding the uncertainty for individual depth increments in quadrature. Analytical uncertainties were low (1.3 %–2.2 %) and the I_{met} uncertainties primarily reflect the uncertainties in ρ, V_f, and in some cases, the inheritance-corrected $^{10}Be_{met}$ concentration. In some cases, uncertainties in the inheritance-corrected $^{10}Be_{met}$ concentrations were large relative to the $^{10}Be_{met}$ concentrations because the difference in concentrations between the two depth increments was small. Hence the Washington Gulch North and Gothic inventories have slightly higher uncertainties relative to the other sites.

Table 3. Environmental variable values and $^{10}Be_{met}$ fluxes at each calibration site.

Site	Elevation[a] (m)	MAP[b] (mm yr^{-1})	Mean snow depth[c] 2018–2019 (m)	Mean SWE[d] 2018–2019 (m)	Inheritance-corrected $^{10}Be_{met}$ inventory $\pm 1\sigma$ uncertainty (10^{10} atoms cm^{-2})	$^{10}Be_{met}$ flux (F_{met}) $\pm 1\sigma$ uncertainty (10^{6} atoms cm^{-2} yr^{-1})
Copper Creek	3476	1353	1.90	0.64	2.35 ± 0.64	1.80 ± 0.50
Washington Gulch North	2944	784	1.01	0.34	1.80 ± 0.57	1.01 ± 0.32
Gothic moraine	2885	885	0.90	0.33	1.27 ± 0.47	0.905 ± 0.339
Washington Gulch South	2864	655	0.80	0.31	1.73 ± 0.34	0.998 ± 0.197
East River terminal	2764	585	0.42	0.19	0.768 ± 0.131	0.431 ± 0.074

[a] elevation (m) from Goulden et al. (2020), [b] mean annual precipitation (MAP) from Mital et al. (2022), [c] mean snow depth (m) from 2018–2019 (Painter, 2018a), and [d] Mean snow water equivalent (SWE) (m) from 2018–2019 (Painter, 2018b).

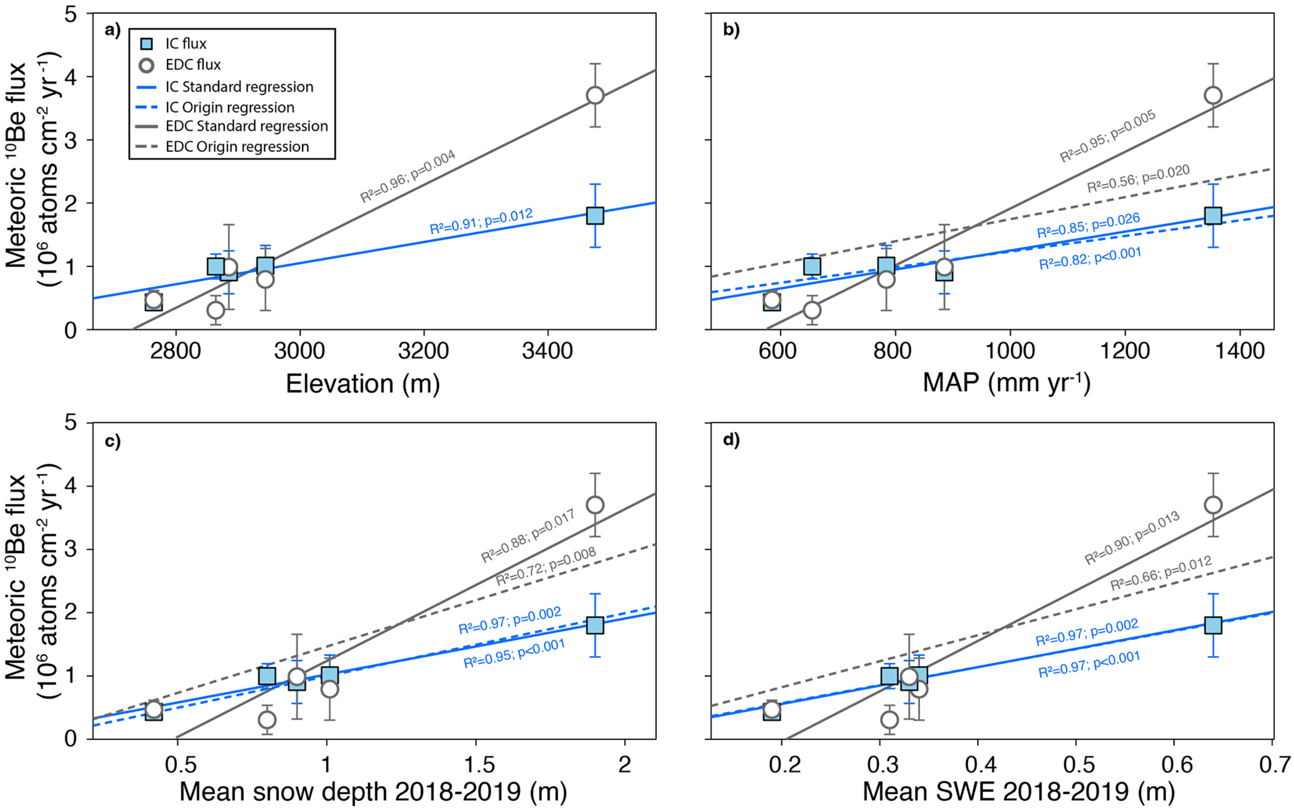

Figure 4. Linear regression models of $^{10}Be_{met}$ flux versus **(a)** elevation, **(b)** mean annual precipitation (MAP), **(c)** mean snow depth (2018–2019), and **(d)** mean snow water equivalent (SWE) (2018–2019). Blue squares show inheritance-corrected fluxes and open gray circles show erosion- and desorption-corrected fluxes. The erosion- and desorption-corrected fluxes use the profile-average desorption model. For the inheritance-corrected (IC) data, solid blue lines show results from standard regression models and the dashed blue lines show regression through the origin models. For the corrected (EDC) data, solid grey lines show standard regression model results and grey dashed lines show regression through the origin models where the y-intercept is zero. Regression through the origin models are shown only for MAP, mean snow depth, and mean SWE. Regression coefficients, R^2 values, and p values are reported in Table S6. Figure S3 and Table S7 report regression results with Copper Creek excluded from the analysis. Figures S4 and S5 show the results from the uppermost and lowermost sample desorption models.

F_{met} and F_{cor} of 1.30×10^6 and 2.04×10^6 atoms cm^{-2} yr^{-1}, respectively. The MAP-based regression resulted in average F_{met} and F_{cor} values of 1.10×10^6 and 1.48×10^6 atoms cm^{-2} yr^{-1} for the standard and 1.11×10^6 and 1.57×10^6 atoms cm^{-2} yr^{-1} for the regression through the origin models, respectively. Snow depth models produced average F_{met} and F_{cor} values of 1.33×10^6 and 2.07×10^6 and 1.34×10^6 and 1.97×10^6 atoms cm^{-2} yr^{-1} for the standard and regression through the origin regression models, respectively. Similarly, SWE-based regressions yielded watershed-averaged F_{met} and F_{cor} values of 1.43×10^6 and 2.34×10^6 for the standard regression and 1.42×10^6 and

Table 4. Modeled erosional, decay, and desorption meteoric ^{10}Be losses and loss-corrected fluxes.

Site	Modeled erosional loss (10^6 atoms cm^{-2} yr^{-1})	Modeled decay loss (10^6 atoms cm^{-2} yr^{-1})	Modeled desorption loss (10^6 atoms cm^{-2} yr^{-1})			$F_{cor} \pm 1\sigma$ uncertainty (10^6 atoms cm^{-2} yr^{-1})		
			upper sample pH	profile-average pH	lowermost sample pH	upper sample pH	profile-average pH	lowermost sample pH
Copper Creek	0.00	0.012	8.51	3.69	0.77	8.52 ± 0.50	3.70 ± 0.50	0.780 ± 0.500
Washington Gulch North	0.55	0.009	1.22	0.23	0.00	1.78 ± 0.49	0.792 ± 0.490	0.560 ± 0.490
Gothic	0.88	0.006	0.99	0.10	0.00	1.88 ± 0.67	0.988 ± 0.670	0.8885 ± 0.670
Washington Gulch South	0.15	0.009	0.16	0.14	0.00	0.318 ± 0.230	0.306 ± 0.230	0.162 ± 0.230
East River Terminal	0.43	0.004	0.54	0.04	0.00	0.969 ± 0.147	0.470 ± 0.147	0.430 ± 0.147

2.05×10^6 atoms cm^{-2} yr^{-1} for the regression through the origin models, respectively. We assessed the influence of extreme values and potential outliers by calculating watershed-averaged F_{met} and F_{cor} values using only pixels with the lowest 99th, 95th, and 90th percentile values, which resulted in lower mean values, with the greatest reductions for the snow-depth and SWE-based estimates (Table 5).

5 Discussion

^{10}Be$_{met}$ profiles tend to have characteristic shapes, and the shapes are sometimes used to infer processes of ^{10}Be$_{met}$ mobility (e.g., Graly et al., 2010). The two most common profile shapes are characterized by either a subsurface peak in concentration or concentrations that decline with depth from a maximum value at the soil surface (Graly et al., 2010). The profile on the East River terminal moraine exhibits an exponential decline in concentration with depth, however the concentrations at the other four sites are fairly uniform with depth. The uniform profiles likely arise from bioturbation, via vegetation or burrowing mammals. Pocket gophers (*Thomomys talpoides*) are the main soil-disturbing mammal within the East River watershed, and soil disturbance can be intense, with surveys indicating soil disturbance by burrowing can exceed one disturbance per m^2 within the elevation range of our sampling sites (Lynn et al., 2018). The distinct stone line at the Copper Creek site may have been generated by bioturbation (e.g., Johnson, 1989), though we cannot rule out the possibility of a periglacial origin (Ball, 1967). The stone line prevented deeper sampling at the Copper Creek site, which makes it difficult to determine whether the full ^{10}Be$_{met}$ inventory was sampled, or whether non-inherited ^{10}Be$_{met}$ is present below the stone line. In either case, the high-elevation Copper Creek site has the highest inventory, which is consistent with the higher precipitation rates at the site.

Glacial moraines erode via diffusive soil transport processes (e.g., Putkonen and Swanson, 2003) and loss of ^{10}Be$_{met}$ due to leaching has been documented or suspected in low pH soils with substantial chemical alteration (e.g., Pavich et al., 1984; Bacon et al., 2012; Dixon et al., 2018). The measured F_{met} values are hence minimum values because erosional and desorption losses of ^{10}Be$_{met}$ reduce inventories. Modeled erosional losses are largest at the Gothic moraine which has the most convex topography, whereas desorption losses are predicted to be greatest at Copper Creek where pH and therefore K_d are estimated to be lowest. The modelling predicts that desorption losses of ^{10}Be$_{met}$ predicted by the profile averaged model tend to be greater than erosional losses, particularly at the Copper Creek site, where predicted desorption losses are about an order of magnitude greater than desorption losses predicted for the other sites. In principle, accounting for erosional, decay, and desorption losses should increase flux estimates relative to the measured

Table 5. Watershed-averaged $^{10}Be_{met}$ flux predictions based on all pixels (100 %) and when excluding pixels with high values by using only the lowest 99th, 95th, and 90th percentile values when calculating the mean.

Variable	Regression type	Meteoric ^{10}Be flux (10^6 atoms cm^{-2} yr^{-1})							
		100 %		99 %		95 %		90 %	
		Inheritance-corrected	Erosion- and desorption-corrected	Inheritance-corrected	Erosion- and desorption-corrected	Inheritance-corrected	Erosion- and desorption-corrected	Inheritance-corrected	Erosion- and desorption-corrected
Elevation (m)	Regular	1.30	2.04	1.29	2.00	1.24	1.86	1.19	1.71
MAP (mm yr^{-1})	Regular	1.10	1.48	1.09	1.45	1.06	1.34	1.02	1.22
	Origin	1.11	1.57	1.11	1.56	1.08	1.52	1.04	1.47
Mean snow depth (m) 2018–2019	Regular	1.33	2.07	1.29	1.96	1.19	1.69	1.11	1.47
	Origin	1.34	1.97	1.29	1.9	1.19	1.74	1.09	1.6
Mean SWE (m) 2018–2019	Regular	1.43	2.34	1.38	2.21	1.26	1.88	1.15	1.59
	Origin	1.42	2.05	1.38	1.99	1.26	1.81	1.15	1.66

Values are calculated by applying regression equations to gridded elevation, mean annual precipitation (MAP), mean snow depth, and mean snow water equivalent (SWE) data to predict a value for each pixel in the watershed and then calculating the average of all pixels.

inheritance-corrected values. However, using Eq. (3) to account for erosion and desorption results in corrected fluxes that are similar to or less than the measured values for all sites except Copper Creek (Tables 3, 4), which suggests that the modeled loss terms may not fully capture true $^{10}Be_{met}$ losses. Although the diffusion coefficient we calculate is comparable to values measured in other landscapes with similar climates (Richardson et al., 2019), there is still inherent uncertainty in using modeled, rather than measured, erosion rates and there is uncertainty in how rates of diffusive soil transport vary with elevation within the East River watershed. There is also uncertainty in the pH-derived K_d values, particularly because the presence of organic compounds, which are abundant in soil, alters sorption relative to experimental systems consisting of only mineral material (Boschi and Willenbring, 2016a, b).

F_{met} is highly correlated with elevation, MAP, snow depth, and SWE, which is unsurprising because these variables are related to one another via orographic controls on precipitation rates. However, different slope and intercept values for regression relationships result in different F_{met} and F_{cor} predictions for the same location and watershed-averaged fluxes that differ by a factor of about two. The precipitation data average over only a few decades and snow depth and SWE datasets cover only two winters, which are only small fractions of the post-glacial period over which $^{10}Be_{met}$ has accumulated in soils. The recent snowfall magnitude may differ from Holocene averages, though the patterns are not likely to have varied substantially, given the orographic controls. However, unlike elevation and MAP datasets, the snow-based inventories yield insight on how local-scale topography may influence spatial patterns of F_{met}. For example, we predict that lower snow accumulation on sharp ridges relative to adjacent slopes leads to lower $^{10}Be_{met}$ accumulation on ridges (Fig. 5). Watershed-averaged fluxes predicted using snow depth and SWE are more sensitive to extreme values than average fluxes based on elevation (Table 5). The mean snow depth of 1.90 m at the highest elevation Copper Creek site is a fraction of the highest snow depth values in the watershed, which exceed 20 m (Fig. S7) and indicates the highest snow depth values are potentially artefacts. The lack of F_{met} calibration sites in areas with higher snow accumulation may result in inaccurate predictions for such areas, however the lack of moraines or other stable, datable landforms at higher elevations makes it difficult to measure $^{10}Be_{met}$ fluxes in such areas. The MAP data are based on decadal-scale precipitation measurements but are interpolated from weather station measurements using elevation as a predictor (Daly et al., 2008). However, the watershed-averaged MAP-based predictions are slightly lower than values based on elevation and snow data. Elevation is the only parameter not subject to temporal bias caused by measurement duration. Hence, given the orographic influences on precipitation within the watershed, elevation should be a robust predictor of $^{10}Be_{met}$ fluxes. However, elevation-based predictions may be biased where local topography leads to persistent snow redistribution via wind and avalanches. Given the different $^{10}Be_{met}$ flux predictions from the elevation, MAP, snow depth, and SWE datasets, an ensemble approach may be appropriate for using $^{10}Be_{met}$ values to quantify surface process rates, in a manner similar to assessing results from multiple production rate scaling models when determining $^{10}Be_{in\ situ}$ exposure ages (e.g., Balco et al., 2008).

Fluxes predicted by an empirical precipitation- and latitude-based model (Graly et al., 2011) are 1.8–3.8 times higher than measured inheritance-corrected fluxes (Fig. 6). The predicted fluxes are 1.0 to 6.0 times higher than the observed erosion- and desorption-corrected values. The empirical formulation of Graly et al. (2011) predicts fluxes as a function of both latitude and precipitation rate. Since our sites have essentially the same latitude, the variability in the predicted fluxes solely represents

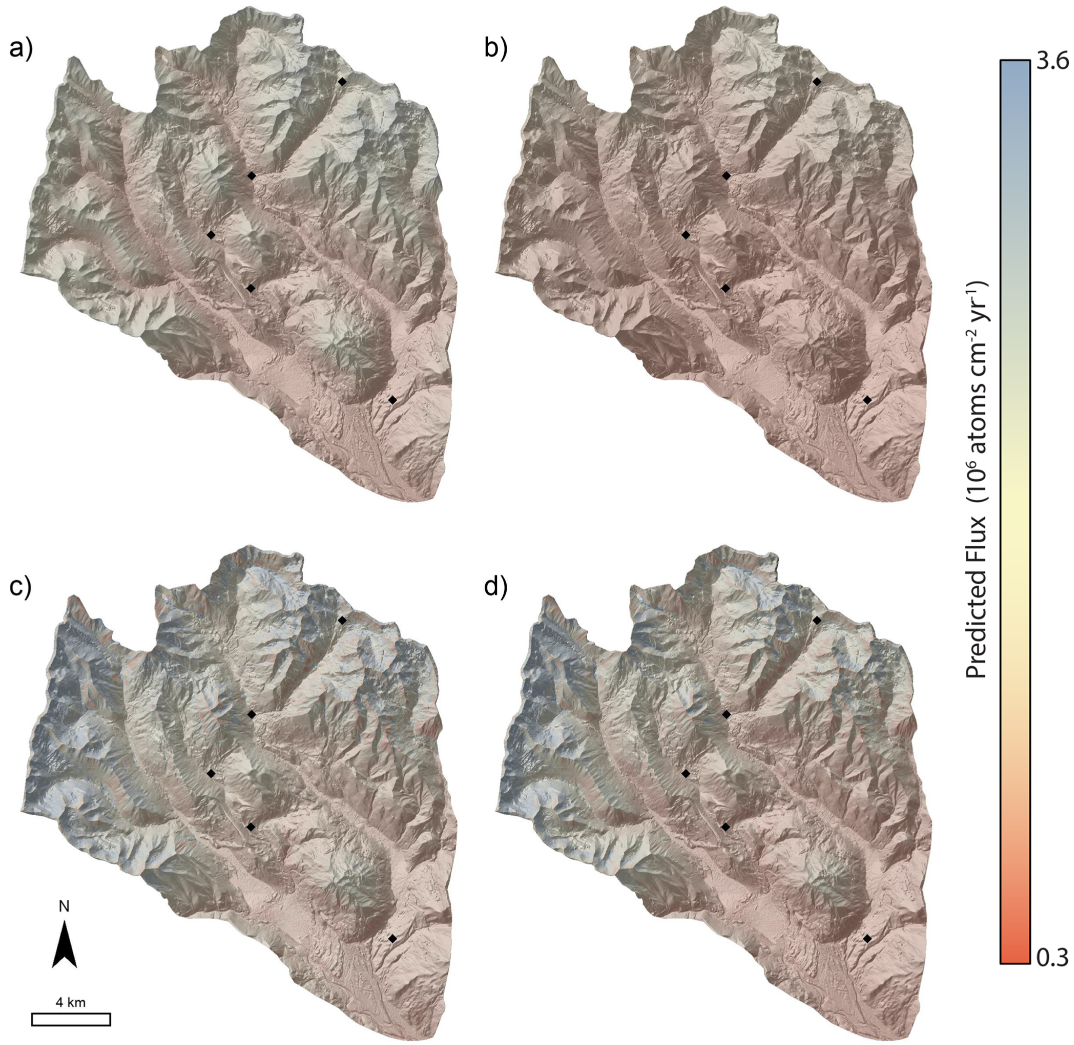

Figure 5. Spatial predictions of $^{10}Be_{met}$ flux based on inheritance-corrected regression models using: **(a)** elevation with the regular regression; **(b)** mean annual precipitation with the origin regression; **(c)** mean snow depth from 2018–2019 with the origin regression; and **(d)** mean snow water equivalent from 2018–2019 with the origin regression. The equivalent results for erosion- and desorption-corrected fluxes calculated using the profile-average desorption model are shown in Fig. S6.

differences in precipitation. Hence the cause of the discrepancy in measured and predicted fluxes may simply reflect a different proportionality between precipitation and flux in the Graly et al. (2011) dataset, which included a worldwide compilation of sites, and the East River dataset. GCM-based models predict $^{10}Be_{met}$ fluxes of 1.46×10^6 atoms cm^{-2} yr^{-1} (Heikkilä and von Blanckenburg, 2015), 1.63×10^6 atoms cm^{-2} yr^{-1}(Zheng et al., 2024, ECHAM6.3-HAM2.3), and 2.12×10^6 atoms cm^{-2} yr^{-1} (Zheng et al., 2024, GEOS-Chem 14.1.1) for the East River watershed and its tributaries (Fig. 7). A single grid-cell from the GCM-models covers an area larger than the watershed, hence the models simulate the influence of meso-scale atmospheric dynamics on $^{10}Be_{met}$ flux, but do not capture within-watershed $^{10}Be_{met}$ variability caused by orographic precipitation. For example, the highest GCM-based flux prediction is 7–13 times greater than the lowest erosion and desorption-corrected flux inferred for the Washington Gulch South site, but our watershed-average predictions only differ from GCM-based predictions by a factor of 1.0 to 1.9. In general, the watershed-averaged predictions from the measured, inheritance-corrected inventories better match GCM-based fluxes than watershed average fluxes corrected for erosion and desorption, which tend to be higher (Fig. 7). An exception is the MAP-based watershed-average flux (1.10–1.57×10^6 atoms cm^{-2} yr^{-1}), which is lower than predictions based on elevation (1.30–2.04×10^6 atoms cm^{-2} yr^{-1}), snow depth (1.33–2.07×10^6 atoms cm^{-2} yr^{-1}), and SWE (1.43–2.34×10^6 atoms cm^{-2} yr^{-1}), which causes the erosion- and desorption-corrected fluxes to better align with the

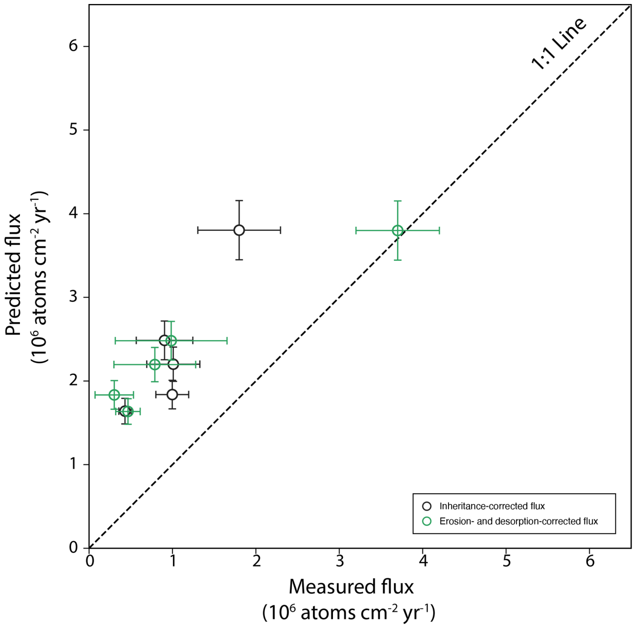

Figure 6. Predicted $^{10}Be_{met}$ flux from the empirical precipitation-based model of Graly et al. (2011), scaled to reflect Holocene-average values (e.g., Clow et al., 2020) versus measured flux values for the five study sites. Measured erosion- and desorption-corrected fluxes use the profile-average desorption model.

GCM-based predictions (Fig. 7). Hence, the GCM-based predictions generally fall within the range of our empirically estimated watershed-averaged flux values, although the degree of agreement depends on the predictor variable and whether or not fluxes are corrected for erosion and desorption.

Soils contain $^{10}Be_{met}$scavenged from the atmosphere by aerosols, but also from dust particles that are derived from aeolian erosion and transported in the atmosphere before being deposited (Monaghan et al., 1986; Graly et al., 2011). The dust-derived or "recycled" $^{10}Be_{met}$ can be as much as $\sim 20\,\%$ of the total flux (Monaghan et al., 1986; Graham et al., 2003). Although the dust contribution to flux estimates does not need to be independently known to quantify surface process rates, provided that time-averaged delivery of dust to soils is representative of the timescale relevant to the surface process rate under investigation, dust contributions should be accounted for before comparing measured fluxes against predictions from GCMs. Hence the comparison of measured $^{10}Be_{met}$ fluxes against the GCM-based predictions is somewhat complicated by the likely contribution of dust to our measured values. The contribution of dust to $^{10}Be_{met}$ inventories in the East River is unconstrained. Contemporary dust fluxes of 5–10 g m^{-2} yr^{-1} have been measured in the San Juan Mountains of Colorado (Lawrence et al., 2010), but recent dust deposition is much greater than average Holocene values (Neff et al., 2008). Long term dust fluxes in the Colorado Front Range are low (Dethier et al., 2012) and dust is thought to contribute $< 10\,\%$ of the total flux of $^{10}Be_{met}$ (Ouimet et al., 2015). If the contribution of dust in the East River is comparable to that in the Front Range, accounting for dust would not substantially influence the magnitude of discrepancies between GCM-based predictions and our empirically derived $^{10}Be_{met}$ flux estimates.

At a regional level, $^{10}Be_{met}$ fluxes for the Colorado Front Range based on soil inventories have been estimated to be $1.5 \pm 0.2 \times 10^6$ atoms cm^{-2} yr^{-1} (Ouimet et al., 2015). Soil inventory-based $^{10}Be_{met}$ fluxes in the Wind River Mountains, Wyoming are $1.46 \pm 0.20 \times 10^6$ and $1.30 \pm 0.48 \times 10^6$ atoms cm^{-2} yr^{-1} for Pinedale- and Bull Lake-aged moraines, respectively (Clow et al., 2020). The 0.43–1.8×10^6 atoms cm^{-2} yr^{-1} F_{met} values and 0.31–3.70×10^6 atoms cm^{-2} yr^{-1} F_{cor} values we measure are consistent with those from the Front Range and Wind River Mountains, though those sites are drier, with ~ 500 mm yr^{-1} of mean annual precipitation in the Front Range (Ouimet et al., 2015) and 276 mm yr^{-1} at the Wind River Mountains sites (Clow et al., 2020), relative to the 585 to 1353 mm yr^{-1} precipitation at the five East River study sites. The driest site in the East River (terminal moraine, 585 mm yr^{-1} MAP) has F_{met} and F_{cor} values of 0.43×10^6 and 0.47×10^6 atoms cm^{-2} yr^{-1}, respectively, which are lower than fluxes inferred in the Front Range and Wind River Mountains. These comparisons suggest that precipitation contributes to regional differences in $^{10}Be_{met}$ flux, but does not explain all of the variability among sites.

Local calibration of $^{10}Be_{met}$ flux greatly increases the utility of $^{10}Be_{met}$ as a tracer of surface processes in the East River watershed, where there is prevalent shale bedrock that is not very amenable to the more common $^{10}Be_{in\ situ}$ method. Our findings show that, whereas $^{10}Be_{met}$ flux predictions from GCM-based models are broadly applicable for large-scale watershed applications, such models do not capture the high spatial variability in $^{10}Be_{met}$ fluxes that is driven by orographic influences on precipitation. Hence using $^{10}Be_{met}$ to quantify physical erosion and weathering rates at the small watershed or soil profile-scale requires not only local-scale calibration of $^{10}Be_{met}$ fluxes, but also a means for predicting $^{10}Be_{met}$ fluxes for sites where elevation and precipitation are different from that of the sites used for calibration. Our study demonstrates how high-resolution LiDAR elevation and snowpack datasets can be combined with locally calibrated $^{10}Be_{met}$ flux measurements to generate spatially resolved flux predictions, which furthers our understanding of the processes that control the delivery of $^{10}Be_{met}$ to soils.

6 Conclusions

Meteoric ^{10}Be fluxes calculated from soil inventories on five glacial moraines dated to 13.0–17.9 ka in the East River watershed, Colorado, USA range from 0.43–1.8×10^6 atoms cm^{-2} yr^{-1} when corrected for inheritance only

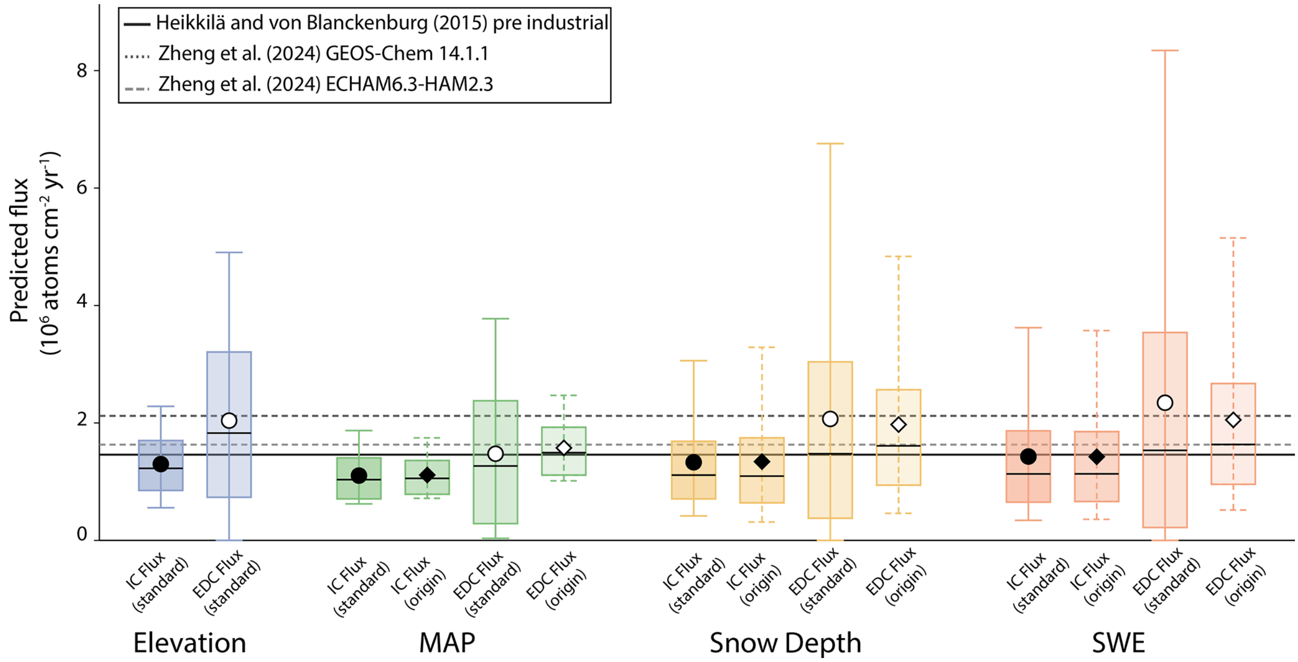

Figure 7. Watershed-scale $^{10}Be_{met}$ fluxes predicted by empirical models based on elevation, mean annual precipitation (MAP), mean snow depth, and mean snow water equivalent (SWE) and flux predictions from global circulation-based (GCM) models. Boxplots show the median (horizontal line), interquartile range, and 5th and 95th percentiles of flux values. Mean fluxes are shown with circles (standard regression models, left box) and diamonds (regression through origin models, right box). GCM-based flux predictions from Heikkilä and von Blanckenburg (2015) and Zheng et al. (2024) are shown as horizontal lines. IC indicates inheritance-corrected fluxes and EDC indicates erosion- and desorption-corrected fluxes calculated using the profile-average desorption model.

and 0.31–3.70 $\times 10^6$ atoms cm^{-2} yr^{-1} after also taking loss of ^{10}Be by erosion and desorption into account. Accounting for pH-dependent desorption substantially increases the estimated flux at the Copper Creek site where soil pH is lowest. The inheritance-corrected and erosion- and desorption-corrected fluxes vary systematically with environmental gradients across the watershed and are generally correlated with elevation, mean annual precipitation, snow depth, and snow water equivalent, reflecting the important role orographic precipitation plays in influencing spatial patterns of meteoric ^{10}Be flux within the watershed. Elevation is the only predictor of flux that is not subject to temporal bias, whereas the snow-based predictions are based on only two years of measurements, and the magnitude and pattern of snow accumulation during those years may vary substantially from Holocene averages. However, the snow-based predictions yield insight into smaller-scale topographic controls on meteoric ^{10}Be fluxes, such as predictions of lower fluxes on sharp ridge crests relative to adjacent hillslopes due to snow redistribution. The fluxes measured at the five moraines are lower by a factor of 1.0 to 6.0 than predictions from an empirical model relating flux and mean annual precipitation and latitude (Graly et al., 2011). Watershed-averaged fluxes predicted from empirical correlations between measured flux and elevation, mean annual precipitation, mean snow depth, and mean snow water equivalent are comparable to predictions from global-scale GCMs. Although the GCM models do not capture the spatial variation in flux within the watershed and are of less utility for soil profile-based applications, the GCM results provide useful estimates of watershed-scale flux. The findings highlight the large degree which meteoric ^{10}Be fluxes vary within alpine landscapes and demonstrate how combining soil meteoric ^{10}Be inventories and high-resolution gridded datasets can generate spatially-resolved meteoric ^{10}Be flux predictions. Our results enhance the utility of meteoric ^{10}Be as a tracer of surface processes in the East River watershed, and other alpine landscapes with rocks that are not conducive to using in situ-produced ^{10}Be and add to our overall understanding of the factors that influence the delivery and retention of meteoric ^{10}Be in soils.

Data availability. Data are available at the U.S. Department of Energy ESS-DIVE archive (https://doi.org/10.15485/3025240; Marmolejo-Cossío et al., 2026).

Supplement. The supplement related to this article is available online at https://doi.org/10.5194/gchron-8-547-2026-supplement.

Author contributions. JM: data curation, formal analysis, investigation, writing (original draft preparation); IL: conceptualization, funding acquisition, investigation, methodology, project administration, resources, supervision, writing (original draft preparation, reviewing and editing); EM: formal analysis, data curation, writing (reviewing and editing); AH: formal analysis, writing (reviewing and editing).

Competing interests. The contact author has declared that none of the authors has any competing interests.

Disclaimer. Publisher's note: Copernicus Publications remains neutral with regard to jurisdictional claims made in the text, published maps, institutional affiliations, or any other geographical representation in this paper. The authors bear the ultimate responsibility for providing appropriate place names. Views expressed in the text are those of the authors and do not necessarily reflect the views of the publisher.

Acknowledgements. We thank J. Reithel at the Rocky Mountain Biological Laboratory for securing access to study sites, B. Quirk for assistance sampling, J. Deems for information on snow datasets, M. Winnick for use of a pH probe, and K. Deng and M. Zheng for helpful correspondence. This is LLNL-JRNL-2007359.

Financial support. This research has been supported by the U.S. Department of Energy (grant no. DE-SC0020354 to Isaac J. Larsen). Prepared in part by Lawrence Livermore National Laboratory under Contract DE-AC52-07NA27344.

Review statement. This paper was edited by Hella Wittmann and reviewed by two anonymous referees.

References

Bacon, A. R., Richter, D. D., Bierman, P. R., and Rood, D. H.: Coupling meteoric ^{10}Be with pedogenic losses of ^{9}Be to improve soil residence time estimates on an ancient North American interfluve, Geology, 40, 847–850, https://doi.org/10.1130/G33449.1, 2012.

Balco, G., Stone, J. O., Lifton, N. A., and Dunai, T. J.: A complete and easily accessible means of calculating surface exposure ages or erosion rates from ^{10}Be and ^{26}Al measurements, Quaternary Geochronol., 3, 174–195, https://doi.org/10.1016/j.quageo.2007.12.001, 2008.

Ball, D. F.: Stone pavements in soils of Caernarvonshire, North Wales, J. Soil Sci., 18, 103–108, https://doi.org/10.1111/j.1365-2389.1967.tb01491.x, 1967.

Barg, E., Lal, D., Pavich, M. J., Caffee, M. W., and Southon, J. R.: Beryllium geochemistry in soils: evaluation of ^{10}Be/^{9}Be ratios in authigenic minerals as a basis for age models, Chem. Geol., 140, 237–258, https://doi.org/10.1016/S0009-2541(97)00051-X, 1997.

Bierman, P. R. and Nichols, K. K.: Rock to sediment – slope to sea with ^{10}Be – rates of landscape change, Annu. Rev. Earth Planet. Sci., 32, 215–255, https://doi.org/10.1146/annurev.earth.32.101802.120539, 2004.

Borchers, B., Marrero, S., Balco, G., Caffee, M., Goehring, B., Lifton, N., Nishiizumi, K., Phillips, F., Schaefer, J., and Stone, J.: Geological calibration of spallation production rates in the CRONUS-Earth project, Quaternary Geochronol., 31, 188–198, https://doi.org/10.1016/j.quageo.2015.01.009, 2016.

Boschi, V. and Willenbring, J. K.: The effect of pH, organic ligand chemistry and mineralogy on the sorption of beryllium over time, Environ. Chem., 13, 711–722, https://doi.org/10.1071/EN15107, 2016a.

Boschi, V. and Willenbring, J. K.: Beryllium desorption from minerals and organic ligands over time, Chem. Geol., 439, 52–58, https://doi.org/10.1016/j.chemgeo.2016.06.009, 2016b.

Brown, L.: Applications of Accelerator Mass Spectrometry, Annu. Rev. Earth Planet. Sci., 12, 39-59, https://doi.org/10.1146/ANNUREV.EA.12.050184.000351, 1984.

Brown, L.: ^{10}Be: Recent applications in Earth sciences, Philos. T. R. Soc. Lond. A, 323, 75–86, 1987a.

Brown, L.: ^{10}Be as a tracer of erosion and sediment transport, Chem. Geol. Isotope Geoscience Section, 65, 189–196, https://doi.org/10.1016/0168-9622(87)90002-9, 1987b.

Brown, L., Pavich, M. J., Hickman, R. E., Klein, J., and Middleton, R.: Erosion of the eastern United States observed with ^{10}Be, Earth Surface Process. Land., 13, 441–457, https://doi.org/10.1002/esp.3290130509, 1988.

Brown, L., Stensland, G. J., Klein, J., and Middleton, R.: Atmospheric deposition of ^{7}Be and ^{10}Be, Geochim. Cosmochim. Ac., 53, 135–142, https://doi.org/10.1016/0016-7037(89)90280-9, 1989.

Campforts, B., Vanacker, V., Vanderborght, J., Baken, S., Smolders, E., and Govers, G.: Simulating the mobility of meteoric ^{10}Be in the landscape through a coupled soil-hillslope model (Be2D), Earth Planet. Sc. Lett., 439, 143–157, https://doi.org/10.1016/j.epsl.2016.01.017, 2016.

Chmeleff, J., von Blanckenburg, F., Kossert, K., and Jakob, D.: Determination of the ^{10}Be half-life by multicollector ICP-MS and liquid scintillation counting, Nuclear Instruments and Methods in Physics Research Section B: Beam Interactions with Materials and Atoms, 268, 192–199, https://doi.org/10.1016/j.nimb.2009.09.012, 2010.

Clow, T., Willenbring, J. K., Schaller, M., Blum, J. D., Christl, M., Kubik, P. W., and von Blanckenburg, F.: Calibrating a long-term meteoric ^{10}Be delivery rate into eroding western US glacial deposits by comparing meteoric and in situ produced ^{10}Be depth profiles, Geochronology, 2, 411–423, https://doi.org/10.5194/gchron-2-411-2020, 2020.

Daly, C., Halbleib, M., Smith, J. I., Gibson, W. P., Doggett, M. K., Taylor, G. H., Curtis, J., and Pasteris, P. P.: Physiographically sensitive mapping of climatological temperature and precipitation across the conterminous United States, Int. J. Climatol., 28, 2031–2064, https://doi.org/10.1002/joc.1688, 2008.

Dannhaus, N., Wittmann, H., Krám, P., Christl, M., and von Blanckenburg, F.: Catchment-wide weathering and erosion rates of mafic, ultramafic, and granitic rock from cosmogenic meteoric

$^{10}Be/^{9}Be$ ratios, Geochim. Cosmochim. Ac., 222, 618–641, https://doi.org/10.1016/j.gca.2017.11.005, 2018.

Deng, K., Wittmann, H., and von Blanckenburg, F.: The depositional flux of meteoric cosmogenic ^{10}Be from modeling and observation, Earth Planet. Sc. Lett., 550, 116530, https://doi.org/10.1016/J.EPSL.2020.116530, 2020a.

Deng, K., Yang, S., von Blanckenburg, F., and Wittmann, H.: Denudation rate changes along a fast-eroding mountainous river with slate headwaters in Taiwan from ^{10}Be (meteoric)/^{9}Be ratios, J. Geophys. Res.-Earth Surf., 125, e2019JF005251, https://doi.org/10.1029/2019JF005251, 2020b.

Deng, K., Wittmann, H., Hsieh, M. L., Yang, S., and von Blanckenburg, F.: Deposition and retention of meteoric ^{10}Be in Holocene Taiwan river terraces, Quaternary Sci. Rev., 265, 107048, https://doi.org/10.1016/j.quascirev.2021.107048, 2021a.

Deng, K., Wittmann, H., Yang, S., and von Blanckenburg, F.: The upper limit of denudation rate measurement from cosmogenic ^{10}Be (meteoric)/^{9}Be ratios in Taiwan, J. Geophys. Res.-Earth Surf., 126, e2021JF006221, https://doi.org/10.1029/2021JF006221, 2021b.

Dethier, D. P., Birkeland, P. W., and McCarthy, J. A.: Using the accumulation of CBD- extractable iron and clay content to estimate soil age on stable surfaces and nearby slopes, Front Range, Colorado, Geomorphology, 173–174, 17–29, https://doi.org/10.1016/j.geomorph.2012.05.022, 2012.

Dixon, J. L., Chadwick, O. A., and Pavich, M. J.: Climatically controlled delivery and retention of meteoric ^{10}Be in soils, Geology, 46, 899–902, https://doi.org/10.1130/G45176.1, 2018.

Dühnforth, M., Anderson, R. S., Ward, D. J., and Blum, A.: Unsteady late Pleistocene incision of streams bounding the Colorado Front Range from measurements of meteoric and in situ ^{10}Be, J. Geophys. Res.-Earth Surf., 117, F01023, https://doi.org/10.1029/2011JF002232, 2012.

Egli, M., Brandová, D., Böhlert, R., Favilli, F., and Kubik, P. W.: ^{10}Be inventories in Alpine soils and their potential for dating land surfaces. Geomorphology, 119, 62–73, https://doi.org/10.1016/J.GEOMORPH.2010.02.019, 2010.

Field, C. V., Schmidt, G. A., Koch, D., and Salyk, C.: Modeling production and climate-related impacts on ^{10}Be concentration in ice cores, J. Geophys. Res.-Atmos., 111, D15107, https://doi.org/10.1029/2005JD006410, 2006.

Foster, M. A., Anderson, R. S., Wyshnytzky, C. E., Ouimet, W. B., and Dethier, D. P.: Hillslope lowering rates and mobile-regolith residence times from in situ and meteoric ^{10}Be analysis, Boulder Creek Critical Zone Observatory, Colorado, Geol. Soc. Am. Bull., 127, 862–878, https://doi.org/10.1130/B31115.1, 2015.

Gaskill, D. L., Godwin, L. H., and Mutschler, F. E.: Geologic map of the Oh-Be-Joyful quadrangle, Gunnison County, Colorado, scale 1 : 24 000, U.S. Geological Survey, Geologic Quadrangle, 578, https://doi.org/10.3133/gq578, 1967.

Gaskill, D. L., Mutschler, F. E., Kramer, J. H., Thomas, J. A., and Zahony, S. G.: Geologic map of the Gothic quadrangle, Gunnison County, Colorado, scale 1 : 24 000, U.S. Geological Survey, Geologic Quadrangle, 1689, https://doi.org/10.3133/gq1689, 1991.

Gosse, J. C. and Phillips, F. M.: Terrestrial in situ cosmogenic nuclides: theory and application, Quaternary Sci. Rev., 20, 1475–1560, https://doi.org/10.1016/S0277-3791(00)00171-2, 2001.

Goulden, T., Hass, B., Brodie, E., Chadwick, K. D., Falco, N., Maher, K., Wainwright, H., and Williams, K.: NEON AOP Survey of Upper East River CO Watersheds: LAZ Files, LiDAR Surface Elevation, Terrain Elevation, and Canopy Height Rasters, Watershed Function SFA, ESS-DIVE [data set], https://doi.org/10.15485/1617203, 2020.

Graham, I., Ditchburn, R., and Barry, B.: Atmospheric deposition of ^{7}Be and ^{10}Be in New Zealand rain (1996–98), Geochim. Cosmochim. Ac., 67, 361–373, https://doi.org/10.1016/S0016-7037(02)01092-X, 2003.

Graly, J. A., Bierman, P. R., Reusser, L. J., and Pavich, M. J.: Meteoric ^{10}Be in soil profiles – A global meta-analysis, Geochim. Cosmochim. Ac., 74, 6814–6829, https://doi.org/10.1016/J.GCA.2010.08.036, 2010.

Graly, J. A., Reusser, L. J., and Bierman, P. R.: Short and long-term delivery rates of meteoric ^{10}Be to terrestrial soils, Earth Planet. Sc. Lett., 302, 329–336, https://doi.org/10.1016/j.epsl.2010.12.020, 2011.

Granger, D. E., Lifton, N. A., and Willenbring, J. K.: A cosmic trip: 25 years of cosmogenic nuclides in geology, Geol. Soc. Am. Bull., 125, 1379–1402, https://doi.org/10.1130/B30774.1, 2013.

Harden, J. W., Fries, T. L., and Pavich, M. J.: Cycling of beryllium and carbon through hillslope soils in Iowa, Biogeochemistry, 60, 317–335, https://doi.org/10.1023/A:1020308729553, 2002.

Harte, J. and Shaw, R.: Shifting dominance within a montane vegetation community: results of a climate-warming experiment, Science, 267, 876–880, https://doi.org/10.1126/science.267.5199.876, 1995.

Heflin, S., Abel, M., Biswas, S., Morales, A., Cifelli, R., Sedlar, J., Feldman, D., Chandrasekar, V., and Kennedy, P., 2024. X-band radar and surface-based observations of cold-season precipitation in western Colorado's complex terrain, J. Hydrometeorol., 25, 1501–1523, https://doi.org/10.1175/JHM-D-23-0147.1, 2024.

Heikkilä, U. and von Blanckenburg, F.: The global distribution of Holocene meteoric ^{10}Be fluxes from atmospheric models: Distribution maps for terrestrial Earth's surface applications, GFZ Data Services [data set], https://doi.org/10.5880/GFZ.3.4.2015.001, 2015.

Heikkilä, U., Beer, J., and Alfimov, V.: Beryllium-10 and beryllium-7 in precipitation in Dübendorf (440 m) and at Jungfraujoch (3580 m), Switzerland (1998–2005), J. Geophys. Res.-Atmos., 113, D11104, https://doi.org/10.1029/2007JD009160, 2008.

Hubbard, S. S., Williams, K. H., Agarwal, D., Banfield, J., Beller, H., Bouskill, N., Brodie, E., Carroll, R., Dafflon, B., Dwivedi, D., Falco, N., Faybishenko, B., Maxwell, R., Nico, P., Steefel, C., Steltzer, H., Tokunaga, T., Tran, P. A., Wainwright, H., and Varadharajan, C.: The East River, Colorado, Watershed: A Mountainous Community Testbed for Improving Predictive Understanding of Multiscale Hydrological-Biogeochemical Dynamics, Vadose Zone J., 17, https://doi.org/10.2136/vzj2018.03.0061, 2018.

Jagercikova, M., Cornu, S., Bourlès, D., Antoine, P., Mayor, M., and Guillou, V.: Understanding long-term soil processes using meteoric ^{10}Be: A first attempt on loessic deposits, Quaternary Geochronol., 27, 11–21, https://doi.org/10.1016/j.quageo.2014.12.003, 2015.

Johnson, D. L.: Subsurface stone lines, stone zones, artifact-manuport layers, and biomantles produced by bioturbation via pocket gophers (*Thomomys bottae*), American Antiquity, 54, 370–389, https://doi.org/10.2307/281712, 1989.

Jordan, C. E., Dibb, J. E., and Finkel, R. C.: ^{10}Be/^{7}Be tracer of atmospheric transport and stratosphere-troposphere exchange, J. Geophys. Res.-Atmos., 108, 4234, https://doi.org/10.1029/2002JD002395, 2003.

Jungers, M. C., Bierman, P. R., Matmon, A., Nichols, K., Larsen, J., and Finkel, R.: Tracing hillslope sediment production and transport with in situ and meteoric ^{10}Be, J. Geophys. Res.-Earth Surf., 114, F04020, https://doi.org/10.1029/2008JF001086, 2009.

Korschinek, G., Bergmaier, A., Faestermann, T., Gerstmann, U. C., Knie, K., Rugel, G., Wallner, A., Dillmann, I., Dollinger, G., Von Gostomski, C. L., and Kossert, K.: A new value for the half-life of ^{10}Be by heavy-ion elastic recoil detection and liquid scintillation counting, Nuclear Instruments and Methods in Physics Research Section B: Beam Interactions with Materials and Atoms, 268, 187–191, https://doi.org/10.1016/j.nimb.2009.09.020, 2010.

Krone, L. V., Wittmann, H., and von Blanckenburg, F.: Precipitation control on weathering intensity and depositional flux of Meteoric ^{10}Be revealed from soil profiles along a climate gradient (Chile), Geophys. Res. Lett., 51, e2024GL108825, https://doi.org/10.1029/2024GL108825, 2024.

Kwang, J. S., Thaler, E. A., Quirk, B. J., Quarrier, C. L., and Larsen, I. J.: A landscape evolution modeling approach for predicting three-dimensional soil organic carbon redistribution in agricultural landscapes, J. Geophys. Res.-Biogeo., 127, e2021JG006616, https://doi.org/10.1029/2021JG006616, 2022.

Lal, D. and Peters, B.: Cosmic ray produced radioactivity on the Earth, in: Kosmische Strahlung II/Cosmic rays II, Springer-Verlag, Berlin Heidelberg, 551–612, https://doi.org/10.1007/978-3-642-46079-1_7, 1967.

Lawrence, C. R., Painter, T. H., Landry, C. C., and Neff, J. C.: Contemporary geochemical composition and flux of aeolian dust to the San Juan Mountains, Colorado, United States, J. Geophys. Res.-Biogeo., 115, G03007, https://doi.org/10.1029/2009JG001077, 2010.

Lynn, J. S., Canfield, S., Conover, R. R., Keene, J., and Rudgers, J. A.: Pocket gopher (*Thomomys talpoides*) soil disturbance peaks at mid-elevation and is associated with air temperature, forb cover, and plant diversity, Arct. Antarct. Alp. Res., 50, e1487659, https://doi.org/10.1080/15230430.2018.1487659, 2018.

Mackey, B. H., Roering, J. J., and McKean, J. A.: Long-term kinematics and sediment flux of an active earthflow, Eel River, California, Geology, 37, 803–806, https://doi.org/10.1130/G30136A.1, 2009.

Marmolejo-Cossío, J., Larsen, I., Marder, E., and Hidy, A.: Meteoric ^{10}Be Flux Calibration Data for the East River Watershed, Colorado, USA. Abiotic and Biotic Controls on Chemical Weathering Rates and Solute Generation, ESS-DIVE repository [data set], https://doi.org/10.15485/3025240, 2026.

Masarik, J. and Beer, J.: Simulation of particle fluxes and cosmogenic nuclide production in the Earth's atmosphere, J. Geophys. Res.-Atmos., 104, 12099–12111, https://doi.org/10.1029/1998JD200091, 1999.

McHargue, L. R. and Damon, P. E.: The global beryllium 10 cycle, Rev. Geophys., 29, 141–158, https://doi.org/10.1029/91RG00072, 1991.

McKean, J. A., Dietrich, W. E., Finkel, R. C., Southon, J. R., and Caffee, M. W.: Quantification of soil production and downslope creep rates from cosmogenic ^{10}Be accumulations on a hillslope profile, Geology, 21, 343–346, https://doi.org/10.1130/0091-7613(1993)021<0343:QOSPAD>2.3.CO;2, 1993.

Mital, U., Dwivedi, D., Brown, J. B., and Steefel, C. I.: Downscaled hyper-resolution (400 m) gridded datasets of daily precipitation and temperature (2008–2019) for the East–Taylor subbasin (western United States), Earth Syst. Sci. Data, 14, 4949–4966, https://doi.org/10.5194/essd-14-4949-2022, 2022.

Monaghan, M. C., Krishnaswami, S., and Thomas, J. H.: ^{10}Be concentrations and the long-term fate of particle-reactive nuclides in five soil profiles from California, Earth Planet. Sc. Lett., 65, 51–60, https://doi.org/10.1016/0012-821X(83)90189-9, 1983.

Monaghan, M. C., Krishnaswami, S., and Turekian, K. K.: The global-average production rate of ^{10}Be, Earth Planet. Sc. Lett., 76, 279–287, https://doi.org/10.1016/0012-821X(86)90079-8, 1986.

Monaghan, M. C., McKean, J., Dietrich, W., and Klein, J.: ^{10}Be chronometry of bedrock-to-soil conversion rates, Earth Planet. Sc. Lett., 111, 483–492, https://doi.org/10.1016/0012-821X(92)90198-5, 1992.

Mudd, S. M., Attal, M., Milodowski, D. T., Grieve, S. W., and Valters, D. A.: A statistical framework to quantify spatial variation in channel gradients using the integral method of channel profile analysis, J. Geophys. Res.-Earth Surf., 119, 138–152, 2014.

Neff, J. C., Ballantyne, A. P., Farmer, G. L., Mahowald, N. M., Conroy, J. L., Landry, C. C., Overpeck, J. T., Painter, T. H., Lawrence, C. R., and Reynolds, R. L.: Increasing eolian dust deposition in the western United States linked to human activity, Nat. Geosci., 1, 189–195, https://doi.org/10.1038/ngeo133, 2008.

Nishiizumi, K., Imamura, M., Caffee, M. W., Southon, J. R., Finkel, R. C., and McAninch, J.: Absolute calibration of ^{10}Be AMS standards, Nuclear Instruments and Methods in Physics Research Section B: Beam Interactions with Materials and Atoms, 258, 403–413, https://doi.org/10.1016/j.nimb.2007.01.297, 2007.

Ouimet, W., Dethier, D., Bierman, P., Wyshnytzky, C., Shea, N., and Rood, D. H.: Spatial and temporal variations in meteoric ^{10}Be inventories and long-term deposition rates, Colorado Front Range, Quaternary Sci. Rev., 109, 1–12, https://doi.org/10.1016/J.QUASCIREV.2014.11.003, 2015.

Painter, T.: ASO L4 Lidar Snow Depth 3m UTM Grid. (ASO_3M_SD, Version 1), NASA National Snow and Ice Data Center Distributed Active Archive Center [data set], https://doi.org/10.5067/KIE9QNVG7HP0, 2018a.

Painter, T.: ASO L4 Lidar Snow Water Equivalent 50m UTM Grid. (ASO_50M_SWE, Version 1), NASA National Snow and Ice Data Center Distributed Active Archive Center [data set], https://doi.org/10.5067/M4TUH28NHL4Z, 2018b.

Painter, T. H., Berisford, D. F., Boardman, J. W., Bormann, K. J., Deems, J. S., Gehrke, F., Hedrick, A., Joyce, M., Laidlaw, R., Marks, D., and Mattmann, C.: The Airborne Snow Observatory: Fusion of scanning lidar, imaging spectrometer, and physically-based modeling for mapping snow water equivalent and snow albedo, Remote Sens. Environ., 184, 139–152, https://doi.org/10.1016/j.rse.2016.06.018, 2016.

Pavich, M. J., Brown, L., Klein, J., and Middleton, R.: ^{10}Be accumulation in a soil chronosequence, Earth Planet. Sc. Lett., 68, 198–204, https://doi.org/10.1016/0012-821X(84)90151-1, 1984.

Panovska, S., Poluianov, S., Gao, J., Korte, M., Mishev, A., Shprits, Y. Y., and Usoskin, I.: Effects of global geomagnetic field variations over the past 100,000 years on cosmogenic radionuclide production rates in the Earth's atmosphere, J. Geophys. Res.-Space Phys., 128, e2022JA031158, https://doi.org/10.1029/2022JA031158, 2023.

Portenga, E. W., Bierman, P. R., Trodick, C. D., Greene, S. E., DeJong, B. D., Rood, D. H., and Pavich, M. J.: Erosion rates and sediment flux within the Potomac River basin quantified over millennial timescales using beryllium isotopes, Geol. Soc. Am. Bull., 131, 1295–1311, https://doi.org/10.1130/B31840.1, 2019.

Prather, R. M., Underwood, N., Dalton, R. M., Barr, B., and Inouye, B. D.: Climate data from the Rocky Mountain Biological Laboratory (1975–2022), Ecology, 104, e4153, https://doi.org/10.1002/ecy.4153, 2023.

Putkonen, J. and Swanson, T.: Accuracy of cosmogenic ages for moraines, Quaternary Res., 59, 255–261, https://doi.org/10.1016/S0033-5894(03)00006-1, 2003.

Quirk, B. J., Larsen, I. J., and Hidy, A. J.: Latest Pleistocene glacial chronology and paleoclimate reconstruction for the East River watershed, Colorado, USA, Quaternary Res., 119, 86–98, https://doi.org/10.1017/qua.2024.5, 2024.

Raisbeck, G., Yiou, F., Fruneau, M., Loiseaux, M., Lieuvin, M., Ravel, J. C., and Lorius, C.: Cosmogenic ^{10}Be concentrations in Antarctic ice during the past 30,000 years, Nature, 292, 825–826, https://doi.org/10.1038/292825a0, 1981.

Reusser, L. J. and Bierman, P. R.: Using meteoric ^{10}Be to track fluvial sand through the Waipaoa River basin, New Zealand, Geology, 38, 47–50, https://doi.org/10.1130/G30395.1, 2010.

Reusser, L., Graly, J., Bierman, P., and Rood, D.: Calibrating a long-term meteoric ^{10}Be accumulation rate in soil, Geophys. Res. Lett., 37, L19403, https://doi.org/10.1029/2010GL044751, 2010.

Richardson, P. W., Perron, J. T., and Schurr, N. D.: Influences of climate and life on hillslope sediment transport, Geology, 47, 423–426, https://doi.org/10.1130/G45305.1, 2019.

Roe, G. H.: Orographic precipitation, Annu. Rev. Earth Planet. Sci., 33, 645–671, https://doi.org/10.1146/annurev.earth.33.092203.122541, 2005.

Stone, J. and Balco, G.: Extraction of beryllium-10 from soil by fusion, University of Washington Cosmogenic Nuclide Laboratory, 6 pp., https://depts.washington.edu/cosmolab/chem/fusionmethod.pdf (last access: 31 August 2026), 2004.

Stone, J. O. H.: A rapid fusion method for separation of beryllium-10 from soils and silicates, Geochim. Cosmochim. Ac., 62, 555–561, https://doi.org/10.1016/S0016-7037(97)00340-2, 1998.

Tran, A. P., Rungee, J., Faybishenko, B., Dafflon, B., and Hubbard, S. S.: Assessment of spatiotemporal variability of evapotranspiration and its governing factors in a mountainous watershed, Water, 11, 243, https://doi.org/10.3390/w11020243, 2019.

Tsai, H., Maejima, Y., and Hseu, Z. Y.: Meteoric ^{10}Be dating of highly weathered soils from fluvial terraces in Taiwan, Quaternary Int., 188, 185–196, https://doi.org/10.1016/j.quaint.2007.06.007, 2008.

von Blanckenburg, F., Bouchez, J., and Wittmann, H.: Earth surface erosion and weathering from the ^{10}Be (meteoric)/^{9}Be ratio, Earth Planet. Sc. Lett., 351–352, 295–305, https://doi.org/10.1016/J.EPSL.2012.07.022, 2012.

West, N., Kirby, E., Bierman, P., and Clarke, B. A.: Aspect-dependent variations in regolith creep revealed by meteoric ^{10}Be, Geology, 42, 507–510, https://doi.org/10.1130/G35357.1, 2014.

Willenbring, J. K. and von Blanckenburg, F.: Meteoric cosmogenic Beryllium-10 adsorbed to river sediment and soil: Applications for Earth-surface dynamics, Earth-Sci. Rev., 98, 105–122, https://doi.org/10.1016/J.EARSCIREV.2009.10.008, 2010.

Wittmann, H., von Blanckenburg, F., Dannhaus, N., Bouchez, J., Gaillardet, J., Guyot, J.L., Maurice, L., Roig, H., Filizola, N., and Christl, M.: A test of the cosmogenic ^{10}Be (meteoric)/^{9}Be proxy for simultaneously determining basin-wide erosion rates, denudation rates, and the degree of weathering in the Amazon basin, J. Geophys. Res.-Earth Surf., 120, 2498–2528, https://doi.org/10.1002/2015JF003581, 2015.

Yamagata, T., Nagai, H., Matsuzaki, H., and Narasaki, Y.: Decadal variations of atmospheric ^{7}Be and ^{10}Be concentrations between 1998 and 2014 in Japan, Nuclear Instruments and Methods in Physics Research Section B: Beam Interactions with Materials and Atoms, 455, 265–270, https://doi.org/10.1016/j.nimb.2018.12.029, 2019.

You, C. F., Lee, T., and Li, Y. H.: The partition of Be between soil and water, Chem. Geol., 77, 105–118, https://doi.org/10.1016/0009-2541(89)90136-8, 1989.

Zheng, M., Adolphi, F., Sjolte, J., Aldahan, A., Possnert, G., Wu, M., Chen, P., and Muscheler, R.: Solar Activity of the Past 100 Years Inferred From ^{10}Be in Ice Cores – Implications for Long-Term Solar Activity Reconstructions, Geophys. Res. Lett., 48, e2020GL090896, https://doi.org/10.1029/2020GL090896, 2021.

Zheng, M., Adolphi, F., Ferrachat, S., Mekhaldi, F., Lu, Z., Nilsson, A., and Lohmann, U.: Modeling atmospheric transport of cosmogenic radionuclide ^{10}Be using geos-chem 14.1. 1 and echam6. 3-ham2. 3: Implications for solar and geomagnetic reconstructions, Geophys. Res. Lett., 51, e2023GL106642, https://doi.org/10.1029/2023GL106642, 2024.